Large-Scale Targeted Cause Discovery with Data-Driven Learning

Anonymous authors
Paper under double-blind review

Abstract

We propose a novel machine learning approach for inferring causal variables of a target variable from observations. Our focus is on directly inferring a set of causal factors without requiring full causal graph reconstruction, which is computationally challenging in large-scale systems. The identified causal set consists of all potential regulators of the target variable under experimental settings, enabling efficient regulation when intervention costs and feasibility vary across variables. To achieve this, we train a neural network using supervised learning on simulated data to infer causality. By employing a local-inference strategy, our approach scales with linear complexity in the number of variables, efficiently scaling up to thousands of variables. Empirical results demonstrate superior performance in identifying causal relationships within large-scale gene regulatory networks, outperforming existing methods that emphasize full-graph discovery. We validate our model's generalization capability across out-of-distribution graph structures and generating mechanisms, including gene regulatory networks of E. coli and the human K562 cell line.

1 Introduction

Identifying causal relationships among variables is a fundamental challenge in machine learning, with widespread applications in generative modeling, system explanation, and variable control (Pearl, 2009). Conventional methods have attempted to infer causal structures using statistical tests or by fitting probabilistic models to observations (Spirtes et al., 2001; Chickering, 2002). However, the exponential complexity of causal graphs renders the problem NP-hard (Chickering, 1996), posing significant challenges for large-scale systems (Zanga et al., 2022).

In this study, we propose a scalable method for identifying causal variables of a target variable from observations in large-scale systems, such as gene regulatory networks (GRNs) (Karlebach & Shamir, 2008). Our approach aims to identify both direct and indirect causes that can regulate the target variable under experimental conditions (Figure 1). Rather than reconstructing an entire causal graph, we focus on identifying a set of causal factors, simplifying the estimation process while retaining practical utility. For instance, in GRNs, identifying causal transcription factors of a target gene is crucial for drug development, as it enables regulation of target gene expression (Huynh-Thu et al., 2010). However, interventions on transcription factors differ in feasibility and cost (Martin & Sung, 2018). By identifying not only direct causes but also all relevant causal factors, our approach prioritizes transcription factors that are more accessible and cost-effective to manipulate, thereby streamlining the development process. We introduce this problem setting as ***targeted cause discovery***.

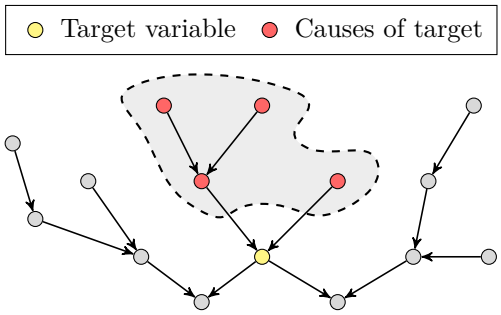

Figure 1: Illustration of targeted cause discovery in a causal graph. Instead of inferring the full causal graph structure, we identify a set of causal variables for a target.

An alternative to our proposed method involves inferring causal variables by traversing the ancestors of a target within a causal graph derived from existing causal discovery techniques. However, estimating complete causal graphs becomes computationally prohibitive for systems with thousands of variables (Zanga et al., 2022). Furthermore, imperfect inference from limited observations leads to error accumulation at each step of ancestral traversal, resulting in exponentially increasing inaccuracies. We explore this issue in greater detail in Section 3.

To overcome these limitations, we propose an end-to-end machine learning approach that directly estimates a set of causal variables from observational and experimental data. Our method trains a deep neural network on simulated data to learn a causal discovery algorithm that generalizes to unseen causal structures (Ke et al., 2023). This data-driven approach allows the model to implicitly capture assumptions embedded in the simulated data. A key advantage of our method is to learn complex causal mechanisms from data, such as differential equations, without requiring explicit formal modeling in score-based causal discovery methods (Chickering, 2002; Zheng et al., 2018). We employ the Transformer architecture for our causal discovery model (Vaswani et al., 2017), building on its demonstrated effectiveness in previous works (Lorch et al., 2022). Nonetheless, the quadratic complexity of Transformer's attention mechanism presents computational challenges. To mitigate this, we introduce a local-inference strategy that scales linearly with the number of variables, enabling efficient application to large-scale problems involving thousands of variables.

Empirical evaluations demonstrate that our method effectively identifies causal relationships within complex systems involving thousands of variables (Section 5). We demonstrate our model's capability to generalize from random causal structures to real-world GRNs, including E. coli, yeast, and the K562 human cell line (Dibaeinia & Sinha, 2020). We further assess the robustness and generalization capability of our approach through comprehensive evaluations on synthetic and real-world datasets, examining various graph structures, causal mechanisms, and noise types, underscoring its applicability in practical scenarios.

2 Preliminary and Related Work

2.1 Problem Formulation

We consider a set of random variables $\mathcal{V} = \{\mathrm{x}_1, \ldots, \mathrm{x}_n\}$ that has a causal structure represented by a directed acyclic graph (DAG), $\mathcal{G} = (\mathcal{V}, \mathcal{E})$. We assume the data-generating process involves no latent variables, and for simplicity, we assume there is no selection bias (Pearl, 2009). The joint distribution $p(\mathcal{V})$ is defined as $\prod_i p(\mathrm{x}_i \mid \mathrm{Pa}(\mathrm{x}_i))$ where $\mathrm{Pa}(\mathrm{x}_i)$ means the set of parent variables of x_i in $\mathcal{G}$. We obtain observations of variables through ancestral sampling.

Definition 1. *Causes for a target node* x_i *is defined as the set of ancestors of* x_i *in* $\mathcal{G}$*, denoted by* $\mathrm{An}(\mathrm{x}_i)$*.*

Definition 2. *A variable* x_j *is a marginal cause of* x_i *if and only if* $\exists c$ *s.t.*

$$p(\mathrm{x}_i \mid \mathrm{do}(\mathrm{x}_j = c)) \neq p(\mathrm{x}_i).$$

The operator $\mathrm{do}(\cdot)$ represents an intervention that fixes specific variables to predefined values during the ancestral sampling process (Pearl, 2009). Specifically, the observation for $\mathcal{V}$ under $\mathrm{do}(\mathrm{x}_j = c)$ follows $\delta_c(\mathrm{x}_j) \prod_{i \neq j} p(\mathrm{x}_i \mid \mathrm{Pa}(\mathrm{x}_i))$, where δ_c is a Dirac delta function at c. Definition 2 implies that interventions on causal variables make a distributional change in the target variable.

Proposition 1. *A set of marginal causes of* x_i *is the subset of* $\mathrm{An}(\mathrm{x}_i)$*.*

We provide the proof for Proposition 1 in Appendix A. This proposition implies that the ancestor set $\mathrm{An}(\mathrm{x}_i)$ forms a necessary condition for identifying variables that influence the target variable x_i in experimental settings. Specifically, in large, sparse networks such as GRNs, efficiently identifying these influential variables can facilitate effective control of target variables. We refer to the task of identifying the set of causes $\mathrm{An}(\mathrm{x}_i)$ of a target variable x_i as *targeted cause discovery.*

2.2 Related Work

Causal discovery Conventional causal discovery methods aim to infer the exact causal graph structure $\mathcal{G}$ from observations (Spirtes et al., 2001; Chickering, 2002). These approaches can be broadly categorized into

constraint-based and score-based methods. Constraint-based methods use conditional independence tests and formalized directional decision rules to identify causal relationships (Spirtes et al., 1995; 2001). However, they require independence testing over combinatorial sets of variables, leading to exponential complexity in the number of variables (Colombo et al., 2014). Subsequent works have sought to reduce this complexity by leveraging sparsity assumptions in causal structures with Gaussian mechanisms (Kalisch & Bühlman, 2007) or by improving computational efficiency through parallelization (Le et al., 2016). Score-based methods, on the other hand, optimize the goodness-of-fit of graph structures while balancing complexity constraints (Chickering, 2002; Hauser & Bühlmann, 2012; Zheng et al., 2018; Brouillard et al., 2020). To navigate the combinatorial search space of causal graphs, these approaches rely on specific assumptions about graph structures and data-generating mechanisms (Lopez et al., 2022). An alternative line of research focuses on estimating the topological ordering of causal variables, which helps reduce optimization complexity (Reisach et al., 2021; Sanchez et al., 2023).

Local approaches To address the computational challenges of estimating full causal graphs, some efforts have focused on inferring the local causal structure of a target node, such as the Markov blanket (Aliferis et al., 2010; Wu et al., 2019), parent set (Gao & Ji, 2015), or parent-cause set (Yin et al., 2008). However, these approaches still suffer from an exponential search space, requiring efficient algorithms for large-scale settings (Gao & Ji, 2015). Magliacane et al. (2016) introduced the problem of estimating ancestral structures. The key difference from our work is that their approach considers the ordering of ancestral nodes (or causes), whereas we do not impose any ordering constraints. By removing the order constraint, we reformulate our training objective as a binary classification task—determining whether a given node is a cause of the target based on observations of all other nodes. This simplification enables us to develop a scalable method for both training and inference.

Learning-based approaches Recent efforts have introduced learning-based approaches that leverage large datasets and computational power for causal discovery (Lopez-Paz et al., 2015; Löwe et al., 2022; Lorch et al., 2022; Ke et al., 2023; Wu et al., 2024). These methods generate synthetic data with known ground-truth causal graphs and train neural networks to infer graph structures from observations (Lorch et al., 2022). In this work, we analyze the generalization performance of these data-driven approaches in large-scale, complex systems. Specifically, we propose a novel strategy that identifies a set of causal variables for a target with linear complexity, enabling efficient scaling to thousands of variables.

3 Targeted Cause Discovery versus Structure Discovery

Targeted cause discovery offers several technical advantages over causal structure discovery, particularly in addressing the shortcomings of conventional methods when the primary objective is to identify the causes of a specific target. In this section, we compare our approach, which directly estimates the set of causes, with an alternative method that infers causes by traversing the ancestors of the target within an estimated causal graph.

1) Error propagation in estimation: With a limited number of observations, causal structure discovery methods have prediction errors (Lorch et al., 2022). When causes are inferred from an inaccurately estimated causal graph, these errors propagate exponentially: If a method has an expected prediction error rate of e per edge, the error rate for estimating causes at a distance d from the target is approximately $1 - (1 - e)^d$. Our approach mitigates this issue by directly inferring causality among distant variables, avoiding the error propagation inherent in graph-based traversal. Figure 2 presents empirical mea-

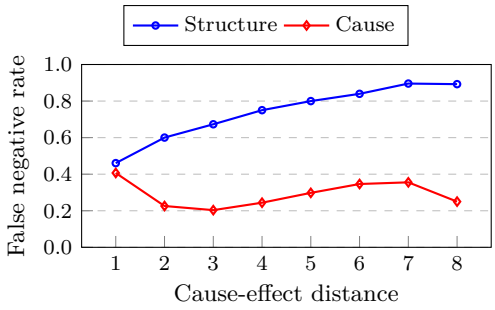

Figure 2: Targeted cause discovery error rate as a function of shortest path length between nodes. *Cause* refers to our method, directly estimating the causes of a target. *Structure* denotes a method that infers causes from an estimated causal graph. Both methods use the same model architecture and dataset but differ in training objectives and inference strategies. Appendix B.6 provides detailed experimental setting.

surements of prediction error rates across different cause-effect distances. The results show that our method maintains a stable error rate regardless of distance, whereas error rates in causal structure discovery methods increase as the cause-effect distance grows.

2) Technical challenges in training: In learning-based causal discovery, neural networks are typically trained to predict the adjacency matrix of a causal structure (Ke et al., 2023; Lorch et al., 2022). However, due to the sparsity of causal graphs, the resulting binary adjacency matrix is highly imbalanced, posing significant training challenges. For instance, in the E. coli GRN, there are only about 2.3 edges per node among 1,565 nodes (Dibaeinia & Sinha, 2020). Such an extreme imbalance is known to hinder neural network training by providing sparse learning signals from the loss function (Kaur et al., 2019). In contrast, our approach trains neural networks to predict ancestors rather than the full adjacency matrix. This formulation mitigates the sparsity issue as shown in Table 1, thereby improving training stability and effectiveness.

Table 1: Averaged ratio of causes (or parents) per node, *i.e.*, $|\mathrm{An}(\mathrm{x})|/n$ (or $|\mathrm{Pa}(\mathrm{x})|/n$). We draw statistics from 10 graphs, each with 1000 nodes and an average in-degree of 2.

Graph type	Parent	Cause
Erdős–Rényi	0.2%	1.1∼1.2%
Scale-free	0.2%	0.4∼2.2%
Gene regulatory	0.2%	0.5∼1.1%

3) Local Inference Guarantee: Targeted cause discovery enables local inference, allowing the identification of causal relationships using only a subset of the system's variables (Proposition 2). Specifically, a cause of a target variable x_i remains a cause within a subsampled variable system (Bongers et al., 2016). This property is particularly useful in large-scale settings, where processing data from all variables is computationally infeasible. Leveraging this property, we propose an efficient algorithm capable of scaling to thousands of variables, as detailed in Section 4.2. It is worth noting that local inference is non-trivial for causal structure discovery, as the direct causal structure can change within a subsampled variable system. We provide a proof of this proposition in Appendix A.

Proposition 2. *For any variable subset $V \subset \mathcal{V}$ s.t. containing x_i and all root variables in $\mathcal{G}$, let $\mathrm{An}(\mathrm{x}_i; V)$ denote the set of ancestors of x_i in the system consisting of V, following the marginalization rule of Bongers et al. (2016). Similarly, let $\mathrm{Pa}(\mathrm{x}_i; V)$ denote the set of parents of x_i within V. Then, $\mathrm{An}(\mathrm{x}_i; V) = \mathrm{An}(\mathrm{x}_i) \cap V$. However, a counterexample exists for parents: $\mathrm{Pa}(\mathrm{x}_i; V) \neq \mathrm{Pa}(\mathrm{x}_i) \cap V$.*

4 Method

In this section, we present our method for Targeted Cause Discovery with Data-driven Learning, termed ***TCD-DL***. We consider a system with n variables $\mathcal{V} = \{\mathrm{x}_1, \ldots, \mathrm{x}_n\}$ having an underlying causal structure $\mathcal{G}$. We denote the observation data as $X \in \mathbb{R}^{n \times m}$, where m is the number of observation samples. In the interventional setting, we define a boolean matrix $M \in \{0, 1\}^{n \times m}$, where 1 indicates the occurrence of interventions.

Our objective is as follows: Given a target variable $\mathrm{x}_i \in \mathcal{V}$, predict a label $l_i \in \{0, 1\}^n$ from the observation X and intervention matrix M, where $l_i[j] = 1$ indicates that x_j is a cause of x_i, *i.e.*, $\mathrm{x}_j \in \mathrm{An}(\mathrm{x}_i)$. We adopt a binary labeling approach, disregarding proximity in the causal graph, as quantifying causal contributions based on proximity is non-trivial. To tackle this problem probabilistically, we estimate a continuous ***cause score*** vector $s_i \in \mathbb{R}^n$, where $s_i[j]$ represents the unnormalized likelihood of x_j being a cause of x_i. A higher score corresponds to a greater likelihood of causality. This continuous relaxation enables the use of gradient-based optimization techniques, which are well-suited for large-scale settings (Bottou, 2010). To obtain a set of estimated causes, we apply thresholding to s_i, considering values greater than zero as causes.

4.1 Data-Driven Learning

A straightforward approach to discovering causality involves conducting interventions on every single variable with a statistically sufficient number of trials to confirm the hypothesis. However, it is often impractical to intervene at every single variable due to experimental limitations and the high costs associated with conducting a sufficient number of trials (Addanki et al., 2020).

To address this challenge, we develop a parameterized model f_θ capable of inferring causality among variables from observations $X \in \mathbb{R}^{n\times m}$ of arbitrarily limited size. Given the target variable index i, the model processes the entire dataset X with intervention matrix M and returns a cause score vector $s_i \in \mathbb{R}^n$ as

$$s_i = f_\theta(X, M, i). \tag{inference}$$

By leveraging observations from all nodes, we can infer causal relationships more accurately than relying solely on the observations of a single pair of variables. We discuss this in more detail in Section 5.4.

We implement f_θ as a deep neural network and train on simulated data $\mathcal{D} = \{(X_k, M_k, \mathcal{G}_k) \mid k \in \mathcal{I}\}$ using a supervised learning approach. Here, $\mathcal{I}$ denotes an index set, and X_k represents an observation dataset sampled from a synthetic causal graph $\mathcal{G}_k$ with an intervention matrix M_k. We generate synthetic datasets using a simulator on random graphs, as detailed in Section 5. Empirically, we demonstrate that the model generalizes to unseen causal structures and causal mechanisms, achieving strong performance on real-world datasets (Section 5.3). For a causal graph $\mathcal{G}_k$ with n_k variables, we obtain a label $l_{k,i} \in \{0,1\}^{n_k}$ for each variable $i = 1, \ldots, n_k$ using topological sorting. The label is defined such that $l_{k,i}[j] = 1$ if the j-th variable is a cause of the i-th variable in $\mathcal{G}_k$. Our training objective, with prediction $f_\theta(X_k, M_k, i) \in \mathbb{R}^{n_k}$, is

$$\underset{\theta}{\text{minimize}}\ \mathbb{E}_{k\sim\mathcal{I}}\mathbb{E}_{i\sim\{1,\ldots,n_k\}}[\mathcal{L}(f_\theta(X_k, M_k, i), l_{k,i})], \tag{training}$$

where $\mathcal{L}$ is the loss function. In this study, we use binary cross-entropy with logits for $\mathcal{L}$ (Wei et al., 2022), ignoring the loss at the target node's position.

Acyclicity. Our problem focuses on estimating a set of causes rather than inferring the full causal graph structure, and therefore does not require explicitly enforcing an acyclicity constraint. Moreover, our supervised learning approach leverages training labels extracted from a DAG, which contains no cycles. Training on such data provides implicit guidance for our model to generate causal predictions that are consistent and non-contradictory.

Model architecture. The model f_θ comprises two sequential modules, a feature extractor g_θ and a score calculator h, designed to optimize compute efficiency. The feature extractor g_θ processes the stack $[X, M] \in \mathbb{R}^{n\times m\times 2}$ to produce features $F_1, F_2 \in \mathbb{R}^{n\times d}$, where each variable index i corresponds to two d-dimensional features $F_1[i], F_2[i] \in \mathbb{R}^d$. We employ an axial-Transformer as the feature extractor (Ho et al., 2019), a matrix-input variant of Transformers that has been a conventional architecture in prior learning-based approaches (Lorch et al., 2022; Ke et al., 2023). Notably, our framework is compatible with general model architectures designed for matrix-shaped inputs. A detailed description of the model architecture is provided in Appendix B.1.

The score calculator h computes the cause score vector s_i for a target index i using dot-product between features as $h(F_1, F_2, i) = F_1 F_2[i] \in \mathbb{R}^n$, where $F_1 \in \mathbb{R}^{n\times d}$ and $F_2[i] \in \mathbb{R}^d$. To sum up, $f_\theta(X, M, i) = h(g_\theta(X, M), i) = h(F_1, F_2, i)$. The use of a separate feature extractor allows for the reuse of features across multiple target indices i, enhancing training efficiency with batch data processing.

4.2 Local Inference for Scaling Up

The axial Transformer comprises three main operations: two attention layers over each variable and observation dimension, and a feed-forward layer (Ho et al., 2019). For an input $X \in \mathbb{R}^{n\times m}$, the complexities of attention layers are $O(n^2 m)$ and $O(nm^2)$, while the complexity of the feed-forward layer is $O(nm)$. The quadratic complexity of the attention mechanism poses challenges for large inputs in terms of computational time and memory usage. In Appendix B.4, we present a detailed analysis of the experimental scales and discuss the computational challenges.

To address this issue, we propose a local inference strategy (Figure 3), supported by Proposition 2, which estimates the causes of a target variable using subsampled variables and observations. Specifically, we define subsample sizes $n' \ll n$ for variables and $m' \ll m$ for observations, set independently of n and m, based on available computing resources. Given a target variable x_i, we randomly sample a subset of

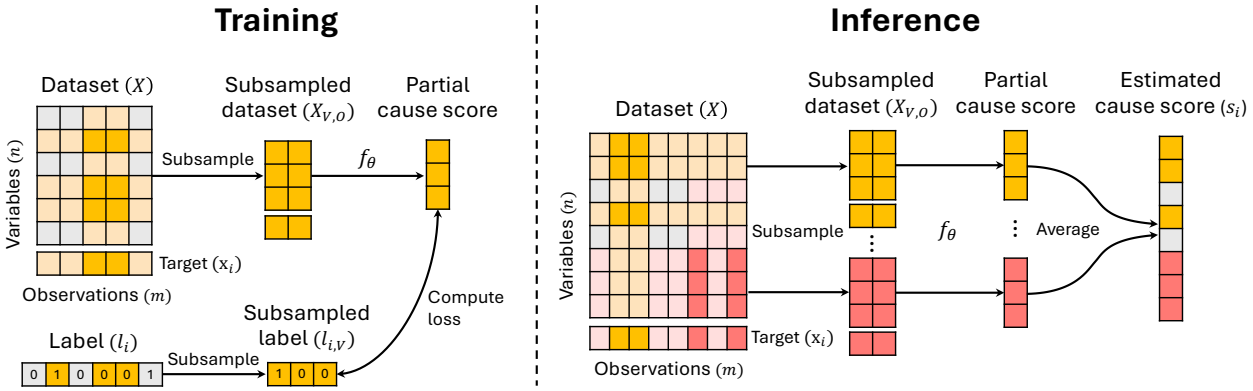

Figure 3: **Overview of our method.** The left figure depicts a single training step, while the right figure illustrates the inference procedure with multiple subsampling and ensembling. Note that the intervention matrix M undergoes the same subsampling as X, resulting in the stacked input $[X_{V,O}, M_{V,O}]$ of shape $n' \times m' \times 2$, which is then fed into the model f_θ. We omit the intervention matrix in the figure for simplicity.

variables $V \subset \mathcal{V}$ with $|V| = n'$, ensuring $\mathrm{x}_i \in V$. We then extract the corresponding observation matrix $X_V \in \mathbb{R}^{n' \times m}$ and intervention matrix $M_V \in \{0,1\}^{n' \times m}$. To avoid distortion from interventions on variables outside the subsampled set V, we select only those observations (columns of X_V) where no variables in $\mathcal{V} \setminus V$ are intervened. From these, we randomly subsample m' observations, yielding $X_{V,O} \in \mathbb{R}^{n' \times m'}$ and $M_{V,O} \in \{0,1\}^{n' \times m'}$, where O denotes the selected observation indices. We denote this subsampling process as $V, O \sim S(X, M, i)$.

We then locally infer the causal effects on x_i from variables in V using $f_\theta(X_{V,O}, M_{V,O}, i) \in \mathbb{R}^{n'}$. Repeating this process across multiple subsamplings of variables and observations, we aggregate and average the results to compute the final cause score vector s_i. For a variable $\mathrm{x}_j \in V$, we denote the estimated cause score to x_i as $f_\theta(X_{V,O}, M_{V,O}, i)[j]$. (Here, j refers to the index in $\mathcal{V}$, but for clarity, we retain the same index notation within V.) The final estimation is then

$$s_i[j] = \mathbb{E}_{V,O \sim S(X,M,i)}\big[f_\theta(X_{V,O}, M_{V,O}, i)[j] \mid \mathrm{x}_j \in V\big]. \qquad \text{(ensembled local-inference)}$$

For training, we apply the identical random subsampling strategy on inputs and target labels. For X_k and a target variable index i, we denote the subsampled data as $X_{k,V,O} \in \mathbb{R}^{n' \times m'}$ and the corresponding target label as $l_{k,i,V} \in \mathbb{R}^{n'}$. The local version of our training objective becomes

$$\underset{\theta}{\text{minimize}} \;\; \mathbb{E}_{k \sim \mathcal{I}} \mathbb{E}_{i \sim \{1,\ldots,n_k\}} \mathbb{E}_{V,O \sim S(X_k, M_k, i)} [\mathcal{L}(f_\theta(X_{k,V,O}, M_{k,V,O}, i), l_{k,i,V})]. \qquad \text{(local training)}$$

We optimize f_θ using stochastic gradient descent with the AdamW optimizer (Loshchilov & Hutter, 2019). Algorithms 1 and 2 describe pseudo codes of our final training and inference algorithms. We leave detailed hyperparameters in Appendix B.2.

Algorithm complexity. Our algorithm reduces the inference complexity from quadratic to linear with respect to the number of variables n. Specifically, we fix the subsample size n' as a constant across all experiments, regardless of the variable size n. By splitting the inputs into fixed-size chunks of n' and repeating the Transformer computation n/n' times, we achieve a computational complexity of $O(n'^2 \cdot n/n') = O(nn')$, reducing the original complexity of $O(n^2)$. Proposition 3 provides a detailed complexity analysis of our inference algorithm, with a proof included in Appendix A.

Proposition 3. *Let n' and m' denote the subsampled variable and observation sizes, and let T denote the ensemble size. For a dataset X with n variables, the inference complexity of our algorithm is $O(nm'T(n' + m'))$.*

Algorithm 1 Training (batch version)

inputs: $\mathcal{D} = \{(X_k, M_k, \mathcal{G}_k) \mid k \in \mathcal{I}\}$
parameters: subsample sizes n' and m', batch size b
initialize θ
repeat
  $\mathcal{X}, \mathcal{Y} \leftarrow \emptyset, \emptyset$
  for $j = 1$ to b **do**
    $k \leftarrow$ sample from $\mathcal{I}$
    $V, O \leftarrow$ subsample given X_k, M_k
    $\mathcal{X} \leftarrow \mathcal{X} \cup \{(X_{k,V,O}, M_{k,V,O}, i) \mid \mathrm{x}_i \in V\}$
    $\mathcal{Y} \leftarrow \mathcal{Y} \cup \{l_{k,i,V} \mid \mathrm{x}_i \in V\}$
  end for
  $\mathbf{g} \leftarrow$ calculate gradients $\nabla_\theta \mathcal{L}(f_\theta(\cdot), \cdot)$ on $\mathcal{X}, \mathcal{Y}$
  $\theta \leftarrow$ update using gradients $\mathbf{g}$
until convergence
return θ

Algorithm 2 Inference

inputs: $X \in \mathbb{R}^{n \times m}$, $M \in \{0,1\}^{n \times m}$, target index i
parameters: subsample sizes n' and m', #ensemble T
initialize $s_i \leftarrow \mathbf{0}_n$
for $t = 1$ to T **do**
  $I \leftarrow \mathrm{permute}(\{1, \ldots, n\} \setminus \{i\})$
  split $I = \cup_{j=1}^{b} I_j$ where $b = \lceil \frac{n}{n'} \rceil$ and $|I_j| \leq n'$
  for $j = 1$ to b **do**
    $I_j \leftarrow I_j \cup \{i\}$ and $V \leftarrow \{\mathrm{x}_k \mid k \in I_j\}$
    $O \leftarrow$ subsample given V, X, M
    $s_i[I_j] \leftarrow s_i[I_j] + f_\theta(X_{V,O}, M_{V,O}, i)$
  end for
end for
$s_i \leftarrow s_i / T$
return s_i

5 Experiment

We present an experimental analysis of out-of-distribution (OOD) settings for targeted causal discovery. In Section 5.2, we verify that our model, trained on random graphs, effectively identifies causal relationships in biological networks consisting of several thousand variables. In Section 5.3, we examine the model's generalization capabilities with respect to novel causal mechanisms and varying noise levels, including analyses on a real-world human gene dataset. Finally, in Section 5.4, we analyze interventional settings and assess sensitivity to hyperparameters. To compare against conventional algorithms such as PC and GIES, we conduct additional small-scale experiments detailed in Appendix C.2.

5.1 Setup

Simulated dataset. We generate the training set $\mathcal{D}$ and test set using the SERGIO GRN simulator (Dibaeinia & Sinha, 2020). This simulator produces single-cell gene expression data, modeling the stochastic nature of transcription based on a user-provided causal graph structure. We conduct experiments over varying levels of simulator's observational fidelity, where higher fidelity yields expression data closer to the population parameters. Details about the simulator, including the generation mechanisms and the definition of fidelity levels, are provided in Appendix B.3. For the training dataset, we use random graph structures including Erdős–Rényi (ER), Scale-Free (SF), and Stochastic Block Model (SBM) with 1,000 variables (Drobyshevskiy & Turdakov, 2019). The test data is generated from biological structures of E. coli (1,565 genes) and yeast (4,441 genes) as obtained from Marbach et al. (2009).

Intervention. We adopt the intervention settings from Lorch et al. (2022). Specifically, we perform single-variable interventions by knocking out gene expressions, *i.e.*, setting their transcription rates to zero. We generate 10 samples per intervention, along with 500 observational samples (details provided in Appendix B.3). In Figure 8, we analyze model performance under various intervention scenarios, including different ratios of intervened nodes and multi-variable interventions.

Identifiability. Our method shares similar identifiability considerations with existing learning-based approaches (Lorch et al., 2022; Ke et al., 2023). In particular, we focus on experimental settings with single-node interventions, where the true causal structure is theoretically identifiable in the limit of infinite interventional data from each variable (Eberhardt et al., 2006). In practice, however, the number of available interventional samples is typically limited, precluding full identifiability guarantees. To address this, we propose a probabilistic framework designed to provide calibrated estimates of causal relationships given the available data, rather than enforcing strict identifiability. This design reflects a practical trade-off, enabling the model to

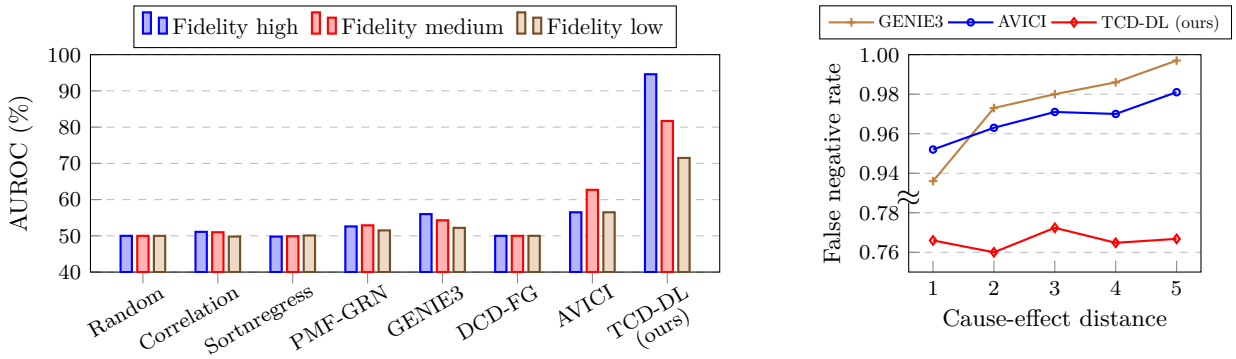

(a) Performance across varying levels of simulator fidelity

(b) Error by causal distance

Figure 4: **Benchmarking results.** (a) Performance on E. coli GRN with 1565 genes over varying levels of simulator's observational fidelity. We provide AUROC, AP, and F1 score values, including standard deviations in Table 10. (b) The cause prediction error rate as a function of the shortest path length between variables in a causal graph.

generate causal predictions that are consistent with observed data, even in low-sample regimes. Empirically, we find that our approach yields meaningful and robust causal inferences under realistic data constraints, as illustrated in Figure 8.

Baseline. We comprehensively evaluate causal discovery methods drawn from various methodological frameworks. As baselines, we include a *random* guessing model, the absolute *correlation* score, and a regression-based method known as *sortnregress* (Reisach et al., 2021). Additionally, we compare against the score-based approach DCD-FG (Lopez et al., 2022), an improved method designed to address instability issues by DCDI (Brouillard et al., 2020) and NO-TEARS (Zheng et al., 2018) in large-scale settings (Kaiser & Sipos, 2022). We evaluate the learning-based approach AVICI (Lorch et al., 2022) by utilizing their released model, which was trained on the same simulator and comparable amount of data as ours. It is worth noting that AVICI closely aligns with the concurrent method CSIVA (Ke et al., 2023), while CSIVA does not provide source code or trained models. Conventional algorithms such as PC and GIES (Spirtes et al., 2001; Hauser & Bühlmann, 2012) are evaluated separately in small-scale experiments due to their limited scalability (Appendix C.2). We assess representative GRN inference methods, including the tree-based method GENIE3 (Huynh-Thu et al., 2010) and the linear factor model PMF-GRN (Skok Gibbs et al., 2024). All mentioned methods, except PC, compute likelihood scores indicative of (direct) causal relationships among variables. We utilize these likelihood scores to construct baseline causal score vectors s_i.

Evaluation metric. We evaluate the targeted cause discovery performance on variables having at least one causal variable. For each target variable, we compare the predicted cause score vector against the ground-truth binary label, where 1 indicates a causal relationship between variables. We employ AUROC, Average Precision (AP), and F1 score for this binary classification task (Rainio et al., 2024). To calculate the F1 score, we threshold the cause scores to match the number of positive predictions with the ground-truth labels. We measure average performance across all valid variables (those with at least one cause) in test datasets. We obtain statistics using expression data with 10 different random seeds for sampling.

5.2 Generalization on Unseen Causal Structure

Benchmarking. Figure 4-a illustrates the performance of targeted causal discovery on the E. coli GRN, which has a novel causal structure not observed during training. Our approach consistently achieves the best performance by a large margin, demonstrating the effectiveness of our data-driven learning approach. The results reveal the shortcomings of existing methods relying on specific assumptions. Linear models (correlation, sortnregress) fail to identify causality in our settings with complex generation mechanisms. As a sanity check, we observe that correlation achieves 70.7% AUROC on causal graphs with linear generation

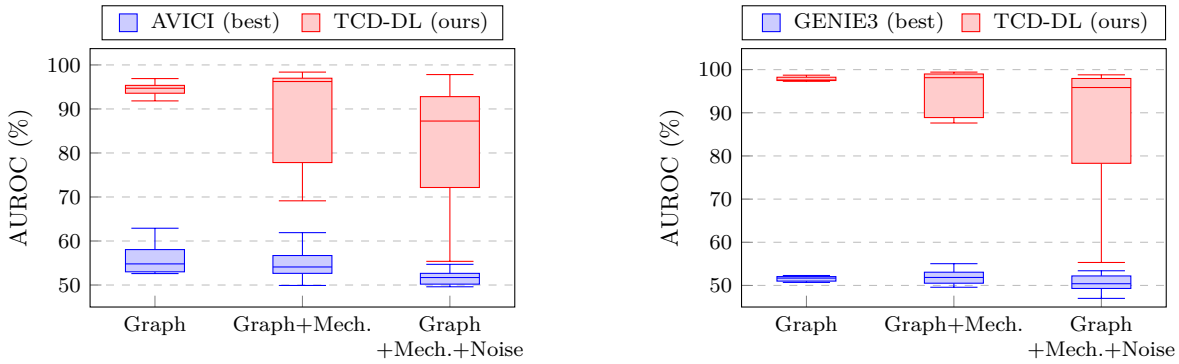

(a) E. coli (b) Yeast

Figure 5: **OOD performance.** Box plots illustrating targeted causal discovery performance on novel graph structures, mechanism parameters (mech.), and noise configurations unseen during training. For the E. coli dataset, AVICI is the best-performing baseline method, whereas GENIE3 achieves the best results for yeast.

mechanisms, showing moderate performance under valid assumptions. The score-based approach (DCD-FG) performs nearly at random, likely due to invalid assumptions about the factorizability of graph structures and simplistic generation mechanisms (Lopez et al., 2022). Our method outperforms the learning-based approach (AVICI), which focuses on direct causality and does not leverage local inference, thereby demonstrating the effectiveness of our scalable algorithm.

Robustness to causal distance. To gain deeper insight into the observed performance improvements, we measure the false-negative rate as a function of the shortest path length in the ground-truth causal graph (Figure 4-b). To ensure a fair comparison, we threshold the causal scores of the best-performing methods so that each produces an identical number of positive predictions. The results indicate that baseline methods exhibit increasing error rates as causal distance grows, whereas our method maintains consistent performance. These findings highlight a key advantage of our approach: it reliably identifies both proximal and distant causes without performance degradation.

Error analysis. While our model demonstrates strong performance, there still remain errors, particularly as simulator fidelity decreases. To investigate the sources of these errors, we compare our model's performance on random graphs sampled from the training setting (*i.e.*, validation set) to its performance on E. coli graphs (*i.e.*, test set). Table 2 reveals that both validation and test performance decline as simulator fidelity decreases. This parallel degradation suggests that the primary source of error is not a generalization issue, but rather stems from other factors. This finding raises questions about causal identifiability in low-fidelity scenarios, indicating that the dataset itself may lack sufficient information for accurate causal inference.

Table 2: AUROC (%) on random graphs (validation) and E. coli GRN (test).

Data \ Fidelity	High	Medium	Low
Validation	92.6	83.3	70.1
Test	94.6	81.7	71.5

Runtime measurement. The runtime of our inference algorithm for processing each target variable is 2.5 seconds for E. coli (1,565 genes) and 7.8 seconds for yeast (4,441 genes), as measured with an NVIDIA RTX 3090 GPU. These results highlight that our model, with ensembled local inference, operates within seconds for large-scale systems. We provide a comparison of the runtime with baseline methods in Appendix C.1, where some baselines, such as DCD-FG and PMF-GRN, take several hours for inference.

5.3 Extened Out-of-Distribution Analysis

OOD simulator configuration. We further study the generalization capabilities of our model by testing on causal mechanism and noise configurations that differ from the training. We adopt the configurations from Lorch et al. (2022), as described in Appendix B.3. Figure 5 shows that our method largely outperforms the baselines across all settings, demonstrating robust generalization. Notably, when only the graph structure

differs from training, our model shows high prediction capability. However, as generation mechanisms diverge from the training setting, the performance variance increases. These findings show both the strengths of our approach and the challenges inherent in generalizing to diverse generation mechanisms.

Real-world human cell analysis. We test our simulator-trained model in a real-world scenario using a Perturb-seq dataset derived from the K562 cell line of a patient with chronic myelogenous leukemia (Replogle et al., 2022). We focus on the gene MYC, a key oncogene involved in cell proliferation, growth, and apoptosis, frequently overexpressed in cancers (Dhanasekaran et al., 2022). We compute cause scores for 1,868 genes and select the top 20 genes as predicted causes of MYC expression (Appendix B.5). One major challenge here is that the exact structure of the human GRN has not yet been fully elucidated. To evaluate our predictions, we compare them with the following three sources: (1) The STRING database, which provides associations between proteins but does not indicate the causal direction (Szklarczyk et al., 2023). (2) Existence of literature that supports causality between a specific gene pair (Table 7). (3) Top 20 genes with the highest expression correlations to MYC. Figure 6 shows that our model demonstrates strong predictive accuracy, achieving 90% precision compared to STRING. Notably, 30% of our predictions are validated by existing literature, demonstrating that our model uncovers meaningful causal relationships. An interesting observation is that only the gene EEF1A1 shows high expression correlation with the target, suggesting that our method identifies novel causal factors not captured by correlation ranking. In Appendix C.3, we provide additional analysis, including the quantitative comparison to correlation ranking and the predicted influence of causal genes. These results highlight our model's potential for real-world applications in understanding and manipulating gene regulation, particularly in the context of personalized medicine and targeted cancer therapies.

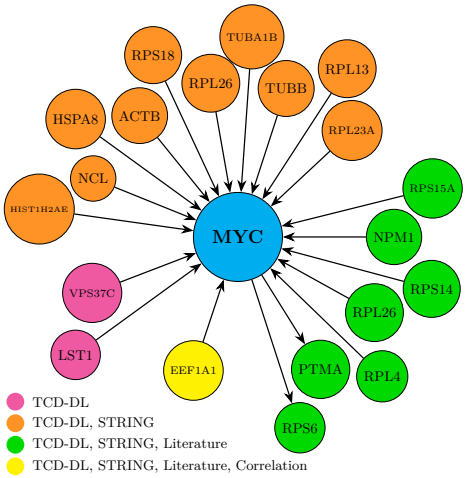

Figure 6: Causal genes of MYC identified by our method. Genes are categorized by validation from STRING, existing literature, and top-20 expression correlations. We note that existing literature validates PTMA and RPS6 as effects of MYC.

Ablating training sources. To further assess the generalization capabilities of our approach, we perform ablation studies by excluding specific causal structures and mechanism types from the training data, and evaluating the resulting models. In Figure 7-a, we conduct experiments with various graph structures, including Erdős–Rényi (ER), directional Scale-Free (SF-direct), Scale-Free (SF), and the Stochastic Block Model (SBM) (Drobyshevskiy & Turdakov, 2019). In Figure 7-b, we vary the causal generation mechanisms to include different analytic functions (linear, non-linear multi-layer perceptron (MLP), polynomial, and sigmoid), while maintaining a scale-free network structure, following Wu et al. (2024).

Figure 7 illustrates the relative performance for each test case, scaled from 0 (random) to 100 (best). Both subfigures exhibit similar patterns, where diagonal entries have relatively lower performance, indicating a generalization gap when the testing data type is omitted from the training sources. Nonetheless, relative performance consistently exceeds 90, highlighting the robust generalization capability of our method. Notably, models trained on a diverse combination of all data types consistently achieve near-optimal performance. This data-scaling effect is consistent with observations from large-scale language models (Brown et al., 2020), suggesting that diversifying training data improves overall causal discovery performance.

5.4 Additional Analysis

Ratio of intervened nodes. We evaluate our model by varying the ratio of intervened nodes and the number of intervention samples per node on the E. coli test dataset. To maintain a fixed dataset size, we adjust the number of observational samples accordingly in each scenario. We select intervened nodes randomly, and use a single model for evaluation across all settings. In this experiment, we disable the dropout effect in the simulator (Appendix B.3), as the random removal of information can weaken interventional signals and lead to misleading analyses.

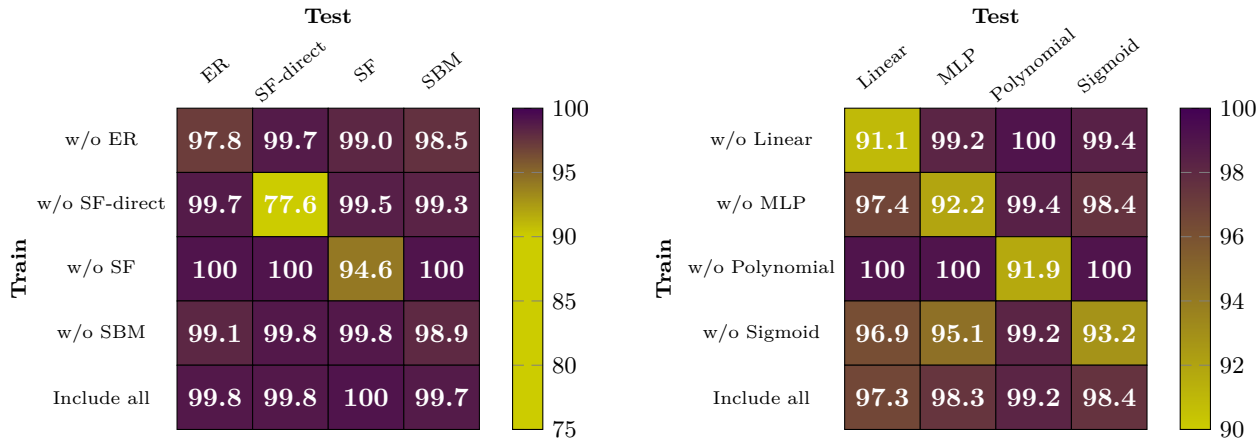

(a) Graph structure

(b) Generation mechanism

Figure 7: **Training source ablation analysis.** The metric used is the relative AUROC, with 100 indicating the best model's performance on each test case and 0 corresponds to random prediction, *i.e.*, $100(p - p_{\text{random}})/(p_{\text{best}} - p_{\text{random}})$, where p denotes the AUROC score of a given model.

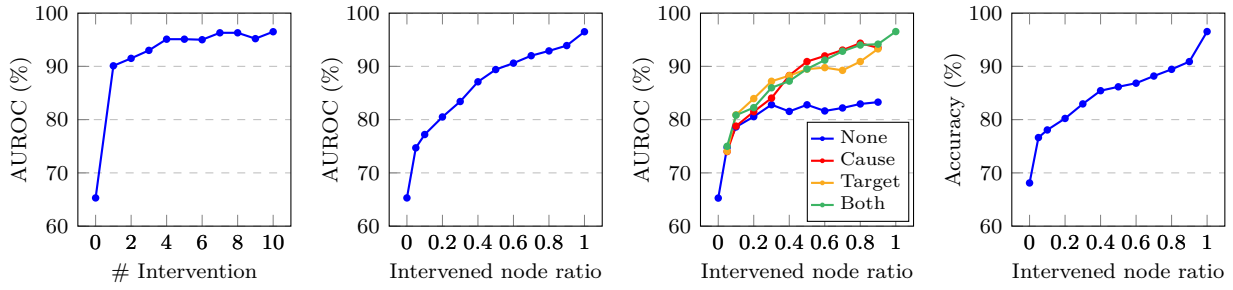

(a) Intervention samples per node

(b) Ratio of intervened nodes

(c) Ratio of intervened nodes (categorized)

(d) Causal direction prediction accuracy

Figure 8: **Intervention analysis.** Performance on the E. coli GRN test dataset with varying intervention settings. (a) Controlling the number of intervention samples per node in the test dataset. (b) Controlling the ratio of intervened nodes among all nodes. A zero ratio indicates that only the observational samples are used. (c) Performance with categorized intervention types. We categorize target nodes into four cases and report average scores for each case: no intervention on the target and ancestors (*None*), intervention on at least one ancestor and not on the target (*Cause*), intervention on the target and not on ancestors (*Target*), and intervention on both (*Both*). (d) Causal direction prediction accuracy of our model across varying ratios of intervened nodes.

From Figure 8-a, we observe that even with only one intervention sample per node (complemented by observational data), the model achieves reasonable performance, reaching an AUROC of 90.1%. As we decrease the ratio of intervened nodes (Figure 8-b), performance decreases sublinearly. These results demonstrate that our method effectively leverages interventional information to infer causality. Furthermore, the model consistently provides meaningful predictions, even with limited intervention data, and surprisingly, performs moderately well with purely observational data, achieving 65.3% AUROC. In Figure 8-c, we present categorized performance based on whether the target node itself or one of its causes has been intervened upon, while varying the ratio of intervened nodes. Interestingly, as indicated by the *None* category in the figure, we observe that even when neither the target node nor its causes are intervened on, the model achieves moderate performance (∼82% AUROC) by leveraging interventional information on other variables.

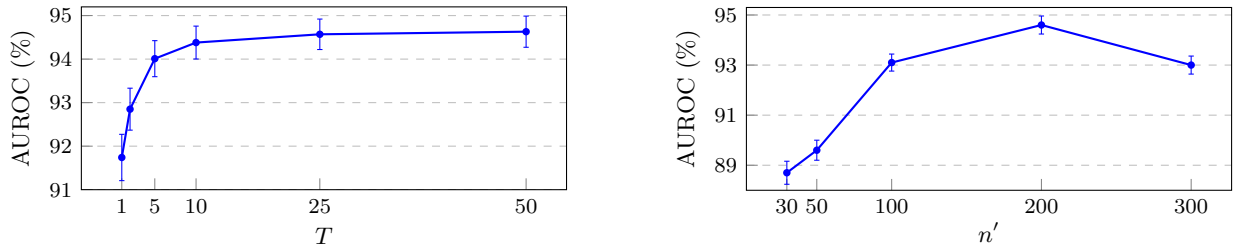

(a) Ensemble size

(b) Subsampled input size

Figure 9: **Hyperparameter analysis.** Performance on E. coli GRN with varying (a) ensemble sizes T and (b) input variable subsample sizes n'.

Multi-node intervention. We conduct experiments involving multi-node interventions by increasing the number of interventions per sample from 1 to 3 during both training and testing while keeping all other configurations unchanged. In this scenario, we observe a slight performance drop from 94.6% to 93.7% AUROC on the E. coli test dataset. We suspect this decline results from increased complexity due to the combinatorial explosion in possible interventions, making it more challenging for the model to fully capture relevant causal information. Nonetheless, exploring optimal intervention settings remains an important direction for future research.

Causal direction prediction. To verify that our model indeed infers causality beyond mere correlation learning, we measure the causal direction prediction accuracy across varying ratios of intervened nodes (Figure 8-d). Specifically, for every pair of nodes i and j with a known causal relationship, we estimated the causal direction by comparing the cause scores $s_i[j]$ and $s_j[i]$ predicted by our model. If $s_i[j] > s_j[i]$, we predicted j as the cause of i. Note that random guessing achieves an accuracy of 50% for this task. As shown in Figure 8-d, our model accurately predicts causal directions under the full-node intervention setting, while achieving 68% accuracy in the observational setting. This clearly demonstrates that our model indeed infers causality beyond mere correlation learning.

Algorithm hyperparameter. We analyze the impact of design choices in our ensembled local-inference strategy by sweeping the ensemble size T and the subsampled variable size n' in Algorithm 2. Figure 9-a demonstrates that performance improves as ensemble size increases, plateauing around 25. This result validates the effectiveness of our ensembled inference approach. Figure 9-b illustrates the effect of subsampled variable size per input. Performance increases with input size up to 200, suggesting that processing larger variable sets through a single Transformer forward pass allows the model to utilize richer relational information. However, performance declines for input sizes exceeding 300, indicating conflicting effects between input complexity and information richness. These results validate our approach of processing a subset of variables, highlighting its effectiveness compared to processing all variables simultaneously.

6 Conclusion and Discussion

In this work, we propose an effective and scalable approach for targeted cause discovery, aiming to identify a set of causal variables for a given target. Our method trains a neural network to learn causal discovery algorithms from simulated data. To handle large-scale systems, we introduce a local-inference strategy that achieves linear complexity with respect to the number of variables. Empirical results on gene regulatory networks demonstrate that our approach significantly outperforms existing causal discovery baselines, exhibiting strong generalization across diverse graph structures and generation mechanisms. By shifting the focus from explicit causal modeling to a data-driven framework, our method aligns with recent advances in deep learning. We anticipate further performance gains through data scaling within our scalable framework. However, our reliance on data-driven black-box models comes at the cost of reduced interpretability. Balancing causal interpretability with the advantages of data-driven methods remains a crucial future direction for targeted cause discovery.

Broader Impact Statement

Our work introduces a scalable technical approach to targeted cause discovery in large-scale causal inference problems, specifically designed for computational efficiency and robustness in identifying relevant causal variables. Positive impacts of our method include improved computational performance and increased accuracy in practical causal inference tasks, enabling researchers to efficiently analyze complex systems such as gene regulatory networks. Although this research primarily advances foundational machine learning techniques without direct societal applications, potential negative impacts might arise if applied irresponsibly—for example, misinterpretation of causal findings leading to incorrect conclusions in biological or medical contexts.

References

Raghavendra Addanki, Shiva Kasiviswanathan, Andrew McGregor, and Cameron Musco. Efficient intervention design for causal discovery with latents. *ICML*, 2020.

Constantin F Aliferis, Alexander Statnikov, Ioannis Tsamardinos, Subramani Mani, and Xenofon D Koutsoukos. Local causal and markov blanket induction for causal discovery and feature selection for classification. *Journal of Machine Learning Research*, 11, 2010.

Jimmy Lei Ba, Jamie Ryan Kiros, and Geoffrey E Hinton. Layer normalization. *arXiv preprint arXiv:1607.06450*, 2016.

Pau Badia-i Mompel, Lorna Wessels, Sophia Müller-Dott, Rémi Trimbour, Ricardo O Ramirez Flores, Ricard Argelaguet, and Julio Saez-Rodriguez. Gene regulatory network inference in the era of single-cell multiomics. *Nature Reviews Genetics*, 24(11):739–754, 2023.

Stephan Bongers, Jonas Peters, Bernhard Schölkopf, and Joris M Mooij. Structural causal models: Cycles, marginalizations, exogenous reparametrizations and reductions. *arXiv preprint arXiv*, 2016.

Léon Bottou. Large-scale machine learning with stochastic gradient descent. *COMPSTAT*, 2010.

Philippe Brouillard, Sébastien Lachapelle, Alexandre Lacoste, Simon Lacoste-Julien, and Alexandre Drouin. Differentiable causal discovery from interventional data. *NeurIPS*, 2020.

Tom Brown, Benjamin Mann, Nick Ryder, et al. Language models are few-shot learners. *NeurIPS*, 2020.

Wenan Chen, Yan Li, John Easton, David Finkelstein, Gang Wu, and Xiang Chen. Umi-count modeling and differential expression analysis for single-cell rna sequencing. *Genome biology*, 19, 2018.

David Maxwell Chickering. Learning bayesian networks is np-complete. *Learning from data: Artificial intelligence and statistics V*, 1996.

David Maxwell Chickering. Optimal structure identification with greedy search. *Journal of machine learning research*, 3, 2002.

Dominique Chu, Nicolae Radu Zabet, and Boris Mitavskiy. Models of transcription factor binding: sensitivity of activation functions to model assumptions. *Journal of Theoretical Biology*, 257, 2009.

Diego Colombo, Marloes H Maathuis, et al. Order-independent constraint-based causal structure learning. *Journal of Machine Learning Research*, 15, 2014.

Jia Deng, Wei Dong, Richard Socher, Li-Jia Li, Kai Li, and Li Fei-Fei. Imagenet: A large-scale hierarchical image database. *CVPR*, 2009.

Renumathy Dhanasekaran, Anja Deutzmann, Wadie D Mahauad-Fernandez, Aida S Hansen, Arvin M Gouw, and Dean W Felsher. The myc oncogene—the grand orchestrator of cancer growth and immune evasion. *Nature reviews Clinical oncology*, 19(1), 2022.

Payam Dibaeinia and Saurabh Sinha. Sergio: a single-cell expression simulator guided by gene regulatory networks. *Cell systems*, 11, 2020.

Alexey Dosovitskiy. An image is worth 16x16 words: Transformers for image recognition at scale. *ICLR*, 2021.

Mikhail Drobyshevskiy and Denis Turdakov. Random graph modeling: A survey of the concepts. *ACM computing surveys (CSUR)*, 52, 2019.

Frederick Eberhardt, Clark Glymour, and Richard Scheines. N-1 experiments suffice to determine the causal relations among n variables. *Innovations in machine learning: theory and applications*, 2006.

Ayako Egoh, Shin Nosuke Kanesashi, Chie Kanei-Ishii, Teruaki Nomura, and Shunsuke Ishii. Ribosomal protein l4 positively regulates activity of ac-myb proto-oncogene product. *Genes to Cells*, 15(8):829–841, 2010.

Brunangelo Falini, Lorenzo Brunetti, Paolo Sportoletti, and Maria Paola Martelli. Npm1-mutated acute myeloid leukemia: from bench to bedside. *Blood, The Journal of the American Society of Hematology*, 136 (15), 2020.

Tian Gao and Qiang Ji. Local causal discovery of direct causes and effects. *NeurIPS*, 2015.

Dalian Gong, Xinxu Rao, Ziqian Min, Xiaowen Liu, Huan Xin, Peijun Zhou, Lifang Yang, and Dan Li. Ube2s targets rpl26 for ubiquitination and degradation to promote non-small cell lung cancer progression via regulating c-myc. *American Journal of Cancer Research*, 13(8), 2023.

Alain Hauser and Peter Bühlmann. Characterization and greedy learning of interventional markov equivalence classes of directed acyclic graphs. *The Journal of Machine Learning Research*, 13, 2012.

Jonathan Ho, Nal Kalchbrenner, Dirk Weissenborn, and Tim Salimans. Axial attention in multidimensional transformers. *arXiv preprint arXiv:1912.12180*, 2019.

Zhe Hong, Chengdang Xu, Shengfeng Zheng, Xinan Wang, Yiran Tao, Yao Tan, Guowen Lin, Denglong Wu, and Dingwei Ye. Nucleophosmin 1 cooperates with brd4 to facilitate c-myc transcription to promote prostate cancer progression. *Cell Death Discovery*, 9(1), 2023.

Vân Anh Huynh-Thu, Alexandre Irrthum, Louis Wehenkel, and Pierre Geurts. Inferring regulatory networks from expression data using tree-based methods. *PloS one*, 5, 2010.

Marcus Kaiser and Maksim Sipos. Unsuitability of notears for causal graph discovery when dealing with dimensional quantities. *Neural Processing Letters*, 2022.

Markus Kalisch and Peter Bühlman. Estimating high-dimensional directed acyclic graphs with the pc-algorithm. *Journal of Machine Learning Research*, 8, 2007.

Guy Karlebach and Ron Shamir. Modelling and analysis of gene regulatory networks. *Nature reviews Molecular cell biology*, 9, 2008.

Harsurinder Kaur, Husanbir Singh Pannu, and Avleen Kaur Malhi. A systematic review on imbalanced data challenges in machine learning: Applications and solutions. *ACM computing surveys (CSUR)*, 52, 2019.

Nan Rosemary Ke, Silvia Chiappa, Jane Wang, Anirudh Goyal, Jorg Bornschein, Melanie Rey, Theophane Weber, Matthew Botvinic, Michael Mozer, and Danilo Jimenez Rezende. Learning to induce causal structure. *ICLR*, 2023.

Thuc Duy Le, Tao Hoang, Jiuyong Li, Lin Liu, Huawen Liu, and Shu Hu. A fast pc algorithm for high dimensional causal discovery with multi-core pcs. *IEEE/ACM transactions on computational biology and bioinformatics*, 16(5):1483–1495, 2016.

Mingli Li, Lu Yang, Anthony KN Chan, Sheela Pangeni Pokharel, Qiao Liu, Nicole Mattson, Xiaobao Xu, Wen-Han Chang, Kazuya Miyashita, Priyanka Singh, et al. Epigenetic control of translation checkpoint and tumor progression via ruvbl1-eef1a1 axis. *Advanced Science*, 10(17), 2023.

Jiayu Liang, Zhihong Liu, Zijun Zou, Xiangxiu Wang, Yongquan Tang, Chuan Zhou, Kan Wu, Fuxun Zhang, and Yiping Lu. Knockdown of ribosomal protein s15a inhibits human kidney cancer cell growth in vitro and in vivo. *Molecular Medicine Reports*, 19(2), 2019.

Yi-Te Lin, Hsing-Pang Lu, and Chuck C-K Chao. Oncogenic c-myc and prothymosin-alpha protect hepatocellular carcinoma cells against sorafenib-induced apoptosis. *Biochemical pharmacology*, 93(1), 2015.

Romain Lopez, Jan-Christian Hütter, Jonathan Pritchard, and Aviv Regev. Large-scale differentiable causal discovery of factor graphs. *NeurIPS*, 2022.

David Lopez-Paz, Krikamol Muandet, Bernhard Schölkopf, and Iliya Tolstikhin. Towards a learning theory of cause-effect inference. *ICML*, 2015.

Lars Lorch, Scott Sussex, Jonas Rothfuss, Andreas Krause, and Bernhard Schölkopf. Amortized inference for causal structure learning. *NeurIPS*, 2022.

Ilya Loshchilov and Frank Hutter. Sgdr: Stochastic gradient descent with warm restarts. *ICLR*, 2017.

Ilya Loshchilov and Frank Hutter. Decoupled weight decay regularization. *ICLR*, 2019.

Sindy Löwe, David Madras, Richard Zemel, and Max Welling. Amortized causal discovery: Learning to infer causal graphs from time-series data. *Conference on Causal Learning and Reasoning*, 2022.

Sara Magliacane, Tom Claassen, and Joris M Mooij. Ancestral causal inference. *Advances in Neural Information Processing Systems*, 2016.

Daniel Marbach, Thomas Schaffter, Claudio Mattiussi, and Dario Floreano. Generating realistic in silico gene networks for performance assessment of reverse engineering methods. *Journal of computational biology*, 16, 2009.

Adam A Margolin, Ilya Nemenman, Katia Basso, Chris Wiggins, Gustavo Stolovitzky, Riccardo Dalla Favera, and Andrea Califano. Aracne: an algorithm for the reconstruction of gene regulatory networks in a mammalian cellular context. In *BMC bioinformatics*, volume 7, pp. 1–15. Springer, 2006.

Erik W Martin and Myong-Hee Sung. Challenges of decoding transcription factor dynamics in terms of gene regulation. *Cells*, 7, 2018.

Judea Pearl. *Causality*. Cambridge university press, 2009.

Oona Rainio, Jarmo Teuho, and Riku Klén. Evaluation metrics and statistical tests for machine learning. *Scientific Reports*, 14, 2024.

Michael J Ravitz, Li Chen, Mary Lynch, and Emmett V Schmidt. c-myc repression of tsc2 contributes to control of translation initiation and myc-induced transformation. *Cancer research*, 67(23), 2007.

Alexander Reisach, Christof Seiler, and Sebastian Weichwald. Beware of the simulated dag! causal discovery benchmarks may be easy to game. *NeurIPS*, 34, 2021.

Joseph M Replogle, Reuben A Saunders, Angela N Pogson, Jeffrey A Hussmann, Alexander Lenail, Alina Guna, Lauren Mascibroda, Eric J Wagner, Karen Adelman, Gila Lithwick-Yanai, et al. Mapping information-rich genotype-phenotype landscapes with genome-scale perturb-seq. *Cell*, 185(14), 2022.

Karen Sachs, Omar Perez, Dana Pe'er, Douglas A Lauffenburger, and Garry P Nolan. Causal protein-signaling networks derived from multiparameter single-cell data. *Science*, 308(5721), 2005.

Pedro Sanchez, Xiao Liu, Alison Q O'Neil, and Sotirios A Tsaftaris. Diffusion models for causal discovery via topological ordering. *ICLR*, 2023.

Claudia Skok Gibbs, Omar Mahmood, Richard Bonneau, and Kyunghyun Cho. Pmf-grn: a variational inference approach to single-cell gene regulatory network inference using probabilistic matrix factorization. *Genome Biology*, 25, 2024.

Peter Spirtes, Clark Glymour, and Richard Scheines. *Causation, prediction, and search*. MIT press, 2001.

Peter L Spirtes, Christopher Meek, and Thomas S Richardson. Causal inference in the presence of latent variables and selection bias. *UAI*, 1995.

Damian Szklarczyk, Rebecca Kirsch, Mikaela Koutrouli, Katerina Nastou, Farrokh Mehryary, Radja Hachilif, Annika L Gable, Tao Fang, Nadezhda T Doncheva, Sampo Pyysalo, et al. The string database in 2023: protein–protein association networks and functional enrichment analyses for any sequenced genome of interest. *Nucleic acids research*, 51(D1), 2023.

Mathias Uhlén, Linn Fagerberg, Björn M Hallström, Cecilia Lindskog, Per Oksvold, Adil Mardinoglu, Åsa Sivertsson, Caroline Kampf, Evelina Sjöstedt, Anna Asplund, et al. Tissue-based map of the human proteome. *Science*, 347(6220), 2015.

Ashish Vaswani, Noam Shazeer, Niki Parmar, Jakob Uszkoreit, Llion Jones, Aidan N Gomez, Łukasz Kaiser, and Illia Polosukhin. Attention is all you need. *NeurIPS*, 2017.

Hongxin Wei, Renchunzi Xie, Hao Cheng, Lei Feng, Bo An, and Yixuan Li. Mitigating neural network overconfidence with logit normalization. *ICML*, 2022.

Rachel B Wilson, Alexandra M Kozlov, Helia Hatam Tehrani, Jessica S Twumasi-Ankrah, Yun Jin Chen, Matthew J Borrelli, Cynthia G Sawyez, Siddhant Maini, Trevor G Shepherd, Robert C Cumming, et al. Elongation factor 1a1 regulates metabolic substrate preference in mammalian cells. *Journal of Biological Chemistry*, 300(3), 2024.

Menghua Wu, Yujia Bao, Regina Barzilay, and Tommi Jaakkola. Sample, estimate, aggregate: A recipe for causal discovery foundation models. *arXiv preprint arXiv:2402.01929*, 2024.

Xingyu Wu, Bingbing Jiang, Kui Yu, Huanhuan Chen, et al. Accurate markov boundary discovery for causal feature selection. *IEEE transactions on cybernetics*, 50(12):4983–4996, 2019.

Jianxin Yin, You Zhou, Changzhang Wang, Ping He, Cheng Zheng, and Zhi Geng. Partial orientation and local structural learning of causal networks for prediction. In *Causation and prediction challenge*, pp. 93–105. PMLR, 2008.

Paul E Young, Rashmi Kanagal-Shamanna, Shimin Hu, Guilin Tang, Beenu Thakral, Naval Daver, Ghayas C Issa, L Jeffrey Medeiros, and Sergej Konoplev. Chronic myeloid leukemia, bcr-abl1-positive, carrying npm1 mutation–first case series from a single institution. *Leukemia Research*, 111, 2021.

Alessio Zanga, Elif Ozkirimli, and Fabio Stella. A survey on causal discovery: theory and practice. *International Journal of Approximate Reasoning*, 151, 2022.

Xun Zheng, Bryon Aragam, Pradeep K Ravikumar, and Eric P Xing. Dags with no tears: Continuous optimization for structure learning. *NeurIPS*, 2018.

Xiang Zhou, Qian Hao, Jun-ming Liao, Peng Liao, and Hua Lu. Ribosomal protein s14 negatively regulates c-myc activity. *Journal of Biological Chemistry*, 288(30), 2013.

A Proofs and Definitions

Proposition 1. *A set of marginal causes of* x_i *is the subset of* $\mathrm{An}(\mathrm{x}_i)$.

Proof. Consider the ancestor structure of node x_i, defined as the subgraph of $\mathcal{G}$ containing the node set $\mathrm{x}_i \cup \mathrm{An}(\mathrm{x}_i)$ and all corresponding edges. We denote this subgraph by $\mathcal{G}_i$. For each node $\mathrm{x}_j \in \mathrm{x}_i \cup \mathrm{An}(\mathrm{x}_i)$, we define the parent set restricted to this subgraph as $\mathrm{Pa}(\mathrm{x}_j \mid \mathcal{G}_i) = \mathrm{Pa}(\mathrm{x}_j) \cap \mathrm{An}(\mathrm{x}_i)$. Under the assumption of no latent variables in $\mathcal{G}$, the joint distribution over the ancestor structure factorizes as follows: $p(\mathrm{x}_i \cup \mathrm{An}(\mathrm{x}_i)) = \prod_{\mathrm{x}_j \in \mathrm{x}_i \cup \mathrm{An}(\mathrm{x}_i)} p(\mathrm{x}_j \mid \mathrm{Pa}(\mathrm{x}_j \mid \mathcal{G}_i))$. For any node $x_k \notin \mathrm{x}_i \cup \mathrm{An}(\mathrm{x}_i)$, a do-operation on x_k does not affect the ancestor structure since the node x_k and all edges connected to x_k are absent from $\mathcal{G}_i$. Also, there are no causal effects on the ancestor set $\mathcal{G}_i$ originating from nodes outside this set. Consequently, for all values c, we have $p(\mathrm{x}_i \mid \mathrm{do}(\mathrm{x}_k = c)) = p(\mathrm{x}_i)$. According to Definition 2, it follows that $x_k \notin \mathrm{x}_i \cup \mathrm{An}(\mathrm{x}_i)$ is not a marginal cause of x_i. This completes the proof by contraposition. □

Proposition 2. *For any variable subset* $V \subset \mathcal{V}$ *s.t. containing* x_i *and all root variables in* $\mathcal{G}$*, let* $\mathrm{An}(\mathrm{x}_i; V)$ *denote the set of ancestors of* x_i *in the system consisting of* V*, following the marginalization rule of Bongers et al. (2016). Similarly, let* $\mathrm{Pa}(\mathrm{x}_i; V)$ *denote the set of parents of* x_i *within* V*. Then,* $\mathrm{An}(\mathrm{x}_i; V) = \mathrm{An}(\mathrm{x}_i) \cap V$*. However, a counterexample exists for parents:* $\mathrm{Pa}(\mathrm{x}_i; V) \neq \mathrm{Pa}(\mathrm{x}_i) \cap V$*.*

Proof. Note that the marginalization rule of Bongers et al. (2016) on a node x_l operates as follows: (1) every direct path $\mathrm{x}_i \to \mathrm{x}_l \to \mathrm{x}_j$ is replaced with a direct edge $\mathrm{x}_i \to \mathrm{x}_j$, and (2) all remaining edges connected to x_l are removed. This marginalization rule preserves all causal relationships (i.e., the existence of a directed path between nodes) after the removal of a node. Therefore, by definition, we have $\mathrm{An}(\mathrm{x}_i; V) = \mathrm{An}(\mathrm{x}_i) \cap V$. In contrast, for direct causes (parents), the relationship may not hold. Consider a causal chain graph with three variables: $\mathrm{x}_1 \to \mathrm{x}_2 \to \mathrm{x}_3$. By definition, $\mathrm{Pa}(\mathrm{x}_3) = \{\mathrm{x}_2\}$. However, in the local system with $V = \{\mathrm{x}_1, \mathrm{x}_3\}$, x_1 becomes the direct cause of x_3, i.e., $\mathrm{Pa}(\mathrm{x}_3; V) = \{\mathrm{x}_1\}$. On the other hand, $\mathrm{Pa}(\mathrm{x}_3) \cap V = \emptyset$. Thus, $\mathrm{Pa}(\mathrm{x}_i; V) \neq \mathrm{Pa}(\mathrm{x}_i) \cap V$. □

Proposition 3 (Algorithm complexity)**.** *Let* n' *and* m' *denote the subsampled variable and observation sizes, and let* T *denote the ensemble size. For a dataset* X *with* n *variables and* m *observations, the inference complexity of our algorithm is* $O(nm'T(n' + m'))$*.*

Proof. The set of n variables can be partitioned into $\lceil \frac{n}{n'} \rceil$ inputs. For each input, the complexities of attention layers are $O(n'^2 m')$ and $O(n' m'^2)$, while the complexity of the feed-forward layers is $O(n'm')$. Thus processing each variable once results in a complexity of $O(\frac{n}{n'}(n'^2 m' + n' m'^2)) = O(nm'(n' + m'))$. Considering an ensemble size of T, the overall computational complexity becomes $O(nm'T(n' + m'))$. □

B Experimental Settings

B.1 Model Architecture

For the feature extractor g_θ, we utilize an axial-Transformer without positional encoding to ensure permutation equivariance (Ho et al., 2019), *i.e.*, if the variables are permuted, the model produces a correspondingly permuted causality prediction. Each Transformer layer comprises two attention layers, one along the variable dimension and one along the observation dimension, followed by a feed-forward layer (Figure 10). Both attention and feed-forward layers include layer normalization and a skip connection (Ba et al., 2016). Detailed configuration is provided in Table 3.

As described in Section 4.1, the input to the Transformer is a stack $[X, M] \in \mathbb{R}^{n \times m \times 2}$, and the output is two feature matrices $F_1, F_2 \in \mathbb{R}^{n \times d}$. In a basic axial Transformer, the output size for an input of size $n \times m \times 2$ is $n \times m \times d$, where d is the embedding dimension (Figure 10). We denote this output as H. To obtain the feature matrix of size $n \times d$, we first average the output H of size $n \times m \times d$ along the observation dimension m, resulting in a matrix of size $n \times d$. We then apply two feed-forward layers and concatenate the results to produce two feature matrices $F_1, F_2 \in \mathbb{R}^{n \times d}$. The total number of trainable parameters of our model is 62k. We will release the code for our model as open-source.

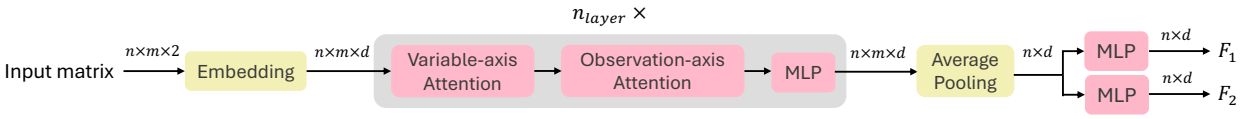

Figure 10: Computational flow of our feature extractor g_θ. We indicate the size of the inputs for each module above the arrows, with only the embedding and pooling modules changing the sizes. For simplicity, normalization and skip connections are excluded from the figure. *MLP* indicates a two-layer perceptron with non-linear activation (Vaswani et al., 2017).

Table 3: Architecture configuration.

Argument	Value
Number of Transformer layers	10
Embedding dimension	16
Number of attention heads	16
Feed-forward layer hidden dimension	96

B.2 Training/Inference Configuration

Training configuration. We train a neural network using the AdamW optimizer (Loshchilov & Hutter, 2019), with training configurations detailed in Table 4. The batch size is chosen to fully utilize our GPU memory (24GB). Training runs for a maximum of 40,000 steps, with early stopping applied if the validation accuracy does not improve over a span of 4,000 steps, checked every 200 steps. The limit of 40,000 training steps is set empirically, as we observed no further performance gains beyond this point on the training dataset specified in Table 6.

We tune the learning rate from the set {6e-4, 8e-4, 1e-3}, finding that 8e-4 yields the most stable training performance across all experimental settings. Notably, the optimal learning rate depends primarily on the model configuration rather than on the dataset type. To further enhance training stability, we apply a cosine learning rate scheduler, which reduces sensitivity to initial learning rates (Loshchilov & Hutter, 2017). Dropout is not used in our experiments, as it empirically decreases performance. We hypothesize that the local training and inference scheme, in which predictions are made based on partial information, inherently reduces the need for dropout regularization.

Inference configuration. Figure 9 describes the configurations required for our inference procedure (Algorithm 2). Hyperparameters are selected based on the analysis in Section 5.4. Note that we use the same sizes, n' and m', during training. The observation size is set to 200, identical to the variable size, to fit within our GPU memory constraints during training.

Computing environment. We conduct all experiments including training and inference, using a NVIDIA RTX 3090 GPU with 24GB memory. The training time for models in Section 5.2 is approximately 9h, while inference takes about a few seconds per target (Table 8).

Table 4: Training configuration.

Argument	Value
Batch size	32
Training step	40,000
Learning rate	8e-4
Learning rate scheduler	cosine
Weight decay	1e-5

Table 5: Inference configuration.

Argument	Value
Subsampled variable size n'	200
Subsampled observation size m'	200
Ensemble size T	50

B.3 GRN Simulator

We use the SERGIO GRN simulator in our experiments (Dibaeinia & Sinha, 2020). Given a user-defined GRN, the simulator generates a gene expression matrix based on a specified cell type configuration.

Generation mechanism. The simulator samples gene expressions from the steady state of a dynamic system modeled as stochastic differential equations (Dibaeinia & Sinha, 2020). Master regulators (*i.e.*, root nodes in the causal graph) operate independently without external regulatory inputs, evolving with fixed production and decay rates. The regulatory influence of each gene is represented by a Hill function with pre-determined interaction parameters (Chu et al., 2009). This mechanism captures non-linear relationships and time-lagged effects, providing a realistic model of gene behavior.

Technical noise. The simulator produces datasets that reflect the statistical properties of real-world single-cell experimental data, incorporating several types of measurement errors and technical noise. The simulator applies these technical noises sequentially to the expression data sampled from the stochastic differential equations:

1. Dropouts: A high proportion of gene expressions (typically 60-95%) are randomly set to zero, simulating the dropout effect common in single-cell technologies.
2. Outlier genes: Some genes are assigned unusually high expression levels, replicating the presence of outliers.
3. Library size: The total expression level for each cell (known as library size) follows a log-normal distribution, reflecting the variability.

Observational fidelity. To generate the unique molecular identifier (UMI) count expression matrix, a quantification scheme in single-cell RNA-sequencing, the simulator applies Poisson random sampling to the expression values λ after incorporating the technical noises (Chen et al., 2018). That is, the final observation value v is derived as $v \sim \text{Poisson}(\lambda)$. To evaluate the impact of this Poisson sampling process on targeted cause discovery performance and to determine the performance ceiling of our method, we control the fidelity of the Poisson sampling and define three levels:

1. High fidelity: Uses expression λ directly as the observation.
2. Medium fidelity: Uses the mean of 100 samples drawn from $\text{Poisson}(\lambda)$.
3. Low fidelity: Uses a single sample drawn from $\text{Poisson}(\lambda)$.

In Figure 4, we analyze the performance differences across varying levels of the simulator's observational fidelity. Unless otherwise specified, we use the high-fidelity setting for our analysis.

Intervention. We use the interventional setting identical to Lorch et al. (2022). Specifically, we perform gene knockout by setting the expression level of a specific gene to zero. We sample 10 intervened observations per gene. For example, given a GRN with 1000 genes, this results in an interventional dataset with 10,000 observations. From these observations and variables, we randomly sample subsets of size $n' = 200$ and $m' = 200$, as provided in Table 5.

B.4 Simulated Dataset

We summarize the configurations of datasets used in our experiments in Table 6, adopted from Lorch et al. (2022). We generate training data using random graphs while testing on biological GRNs, E. coli (1,565 genes) and yeast (4,441 genes), obtained from Marbach et al. (2009). Figure 11 shows the degree histograms of these graph structures, highlighting the different patterns between biological graphs and random graphs. We generate interventional data by performing gene knockout on each gene, obtaining 10 observations per intervention. For yeast, we obtain 5 observations per intervention due to its larger gene count. We include 500 observational data points and conduct inference using a mixture of observational and interventional data. We preprocess each observation matrix using $\log_2$ counts-per-million (CPM) normalization following previous works (Lorch et al., 2022).

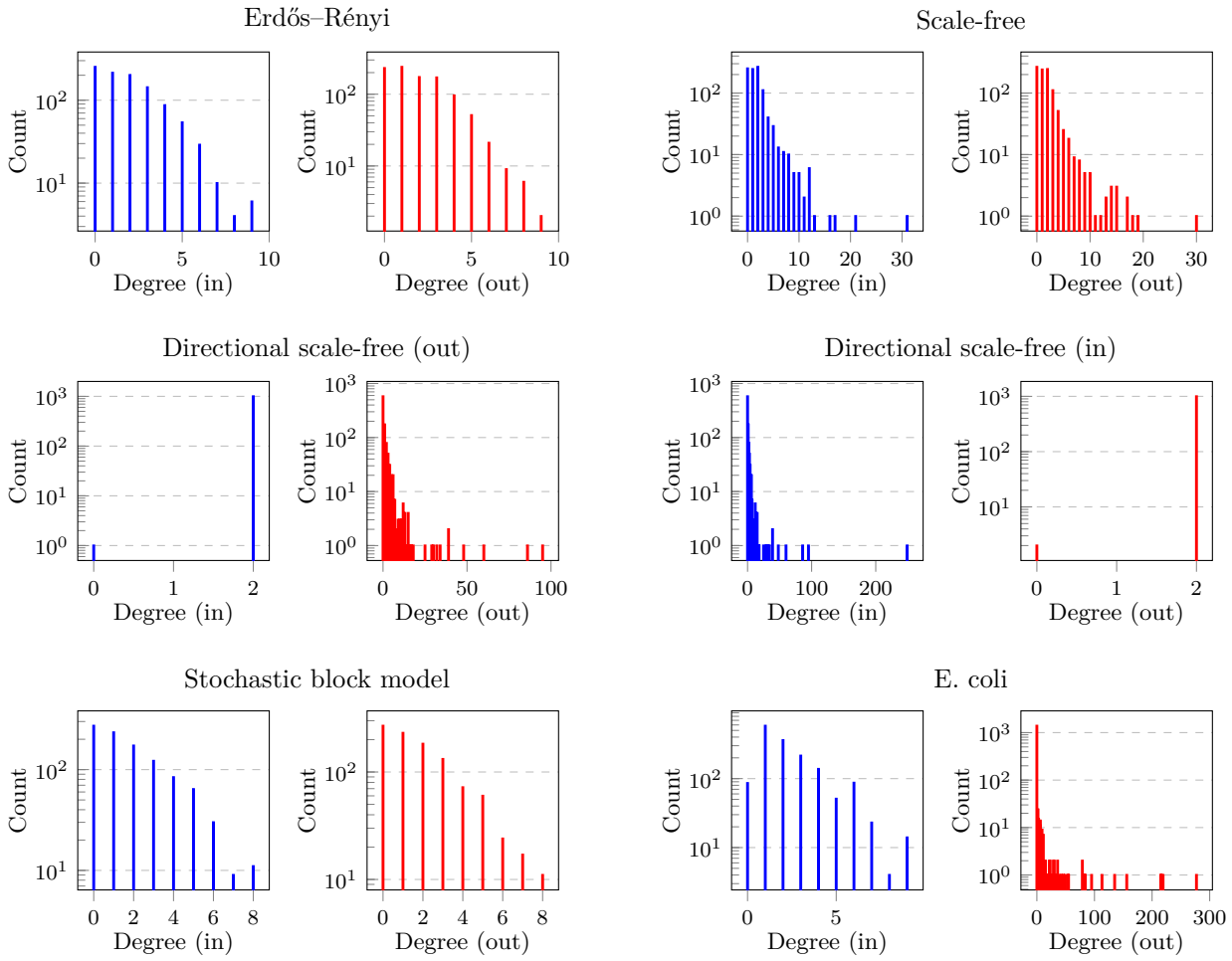

Figure 11: **Edge degree histograms** of graph structures considered in our experiments. All graphs have an average degree of 2. Blue represents the in-degree histogram, and red represents the out-degree histogram.

For the out-of-distribution (OOD) analysis in Figure 5, we adopt configurations from Lorch et al. (2022)-Table 4. These configurations include varying mechanism function parameters, such as Hill function coefficients and decay rates, which differ from the training settings. We also test models on OOD technical noise types, as described in Table 6. These noise types reflect the statistics of different experimental datasets, which have varying dropout percentages, outlier ratios, and library size distributions (Lorch et al., 2022).

Computational challenge. For the yeast dataset, each input comprises approximately 100 million entries—2,000 times larger than the number of pixels in an image from ImageNet (Deng et al., 2009) and 500,000 times larger than the number of input tokens for Vision Transformers (Dosovitskiy, 2021). This substantial size presents significant computational challenges for deep neural networks in memory usage and computation time. To overcome this, we propose a local-inference strategy that efficiently processes datasets across all considered scales.

B.5 Human Cell Dataset

This section describes a Perturb-seq dataset used in the human cell experiments (Figure 6). The dataset contains gene expression data from the K562 cell line, which is derived from a patient with chronic myelogenous leukemia (Replogle et al., 2022). The dataset includes both interventional and observational data on gene expression. The intervention is performed through gene knockouts, identical to our simulation setting.

Table 6: **Dataset configuration.** Note for abbreviations used: ER (Erdős–Rényi), SF (Scale-Free), SF-direct (directional Scale-Free), and SBM (Stochastic Block Model) (Drobyshevskiy & Turdakov, 2019). For the training data, we randomly select the graph structure and edge degree independently from the candidate sets. We use a slash (/) symbol to separately denote the statistics for E. coli and yeast GRNs. For the exact configuration of technical noise, please refer to Table 4 in Lorch et al. (2022).

Argument	Training set	Test set
Graph structure	{ER, SF, SF-direct, SBM}	E. coli/yeast
Average edge degree	{2,4,6}	2.3/2.1
Dataset size $\|\mathcal{D}\|$ per graph structure	150	10
Variable size (n)	1,000	1,565/4,441
Number of observations per intervention	10	10/5
Observation size (interventional)	10,000	15,650/22,205
Observation size (observational)	500	500
Number of cell types	10	10
Technical noise type	10x-chromium	10x-chromium
Technical noise type (OOD)	-	{illumina, drop-seq, smart-seq}

Table 7: Predicted causal gene interactions for target gene MYC by our method. It is worth note that the absence of literature does not imply the invalidation of causality but rather indicates that the causality has not yet been elucidated.

Target gene	Causal gene	Supported by
MYC	EEF1A1	TCD-DL, STRING, Literature (Li et al., 2023; Wilson et al., 2024), Correlation
	NPM1	TCD-DL, STRING, Literature (Hong et al., 2023)
	PTMA	TCD-DL, STRING, Literature (Lin et al., 2015)
	RPL26	TCD-DL, STRING, Literature (Gong et al., 2023)
	RPL4	TCD-DL, STRING, Literature (Egoh et al., 2010)
	RPS14	TCD-DL, STRING, Literature (Zhou et al., 2013)
	RPS15A	TCD-DL, STRING, Literature (Liang et al., 2019)
	RPS6	TCD-DL, STRING, Literature (Ravitz et al., 2007)
	RPL23A	TCD-DL, STRING
	NCL	TCD-DL, STRING
	HSPA8	TCD-DL, STRING
	HIST1H2AE	TCD-DL, STRING
	RPL13	TCD-DL, STRING
	ACTB	TCD-DL, STRING
	TUBB	TCD-DL, STRING
	TUBA1B	TCD-DL, STRING
	RPL26	TCD-DL, STRING
	RPS18	TCD-DL, STRING
	LST	TCD-DL
	VPS37C	TCD-DL

From the Perturb-seq dataset, we obtain 1,868 genes that have undergone intervention. We conduct the inference among these genes. For each intervention, we randomly subsample 10 observations. We also sample 500 observational data points, consistent with the number used in our training setting (Table 6). Using this subsampled dataset, we run our TCD-DL inference algorithm to obtain cause scores for the target gene MYC, applying the same CPM normalization scheme used in our simulation data (Appendix B.3).

B.6 Setting for Error Propagation Analysis

This section details the experimental setup for Figure 2 (Section 3). We generate scale-free random graphs with 100 nodes and define causal mechanisms using a two-layer perceptron with a Tanh activation function (Wu et al., 2024). Root variables are sampled from a uniform distribution. Both approaches—estimating the full causal structure and identifying a set of causal variables—are trained using the same Transformer architecture. However, their final layers are modified to align with their respective objectives. Both methods maintain the same number of model parameters and are trained on datasets of equal size. To enable a clear comparison of how the false negative rate (FNR) evolves with increasing cause-effect distance, we threshold the cause scores to ensure similar FNRs at a cause-effect distance of 1.

C Additional Experimental Results

C.1 Runtime Comparison

Table 8 compares the inference times of methods for targeted cause discovery. Some baseline methods (sortnregress and GENIE3) can individually compute a cause score vector for a target, while other baselines (AVICI, DCD-FG, PMF-GRN) require the calculation of the entire $n \times n$ score matrix to obtain a cause score vector for a target. From the table, our method conducts inference within seconds even for the yeast gene regulatory network (GRN) comprising 4,441 genes. In contrast, certain baselines encounter memory issues (AVICI) or require substantial computation time (DCD-FG, PMF-GRN).

Table 8: **Runtime measurement.** We measure inference time for identifying the causes of a target variable with an NVIDIA RTX 3090 GPU. *OOM* refers to the GPU out-of-memory error.

Species	Sortnregress	GENIE3	AVICI	DCD-FG	PMF-GRN	TCD-DL (ours)
E. coli (1,565 genes)	0.9s	1.7s	3.1s	1h 55m	3h 2m	2.5s
yeast (4,441 genes)	2.8s	2.7s	OOM	98h 31m	10h 46m	7.8s

C.2 Small-Scale Settings

In Table 9, we conduct experiments in small-scale settings, comparing our approach to conventional methods such as PC and GIES (Spirtes et al., 2001; Hauser & Bühlmann, 2012). We train our model exclusively on synthetic datasets generated with randomly parameterized analytic functions (linear, non-linear multi-layer perceptron (MLP), polynomial, and sigmoid), while maintaining a scale-free random network structure with 10 nodes. For testing, we sample datasets with new causal mechanism coefficients and graph structures. Additionally, we evaluate the methods on a real-world dataset called Sachs, which contains 11 variables (Sachs et al., 2005). We obtain interventional data from bnlearn[1], including six intervention types, each applied to a single node. We sample a total of 100 observations for inference.

Given the DAG predicted by baseline methods, we apply topological sorting to obtain binary predictions for ancestor relationships. For our approach, we threshold the cause scores at 0 to obtain binary predictions. After inferring the causal structure, we measure binary classification accuracy for every pair of nodes to determine if the method accurately predicts causal (ancestor) relationships. Table 9 demonstrates that our method generalizes effectively to real-world settings with fewer nodes, highlighting its promising capabilities.

C.3 Analysis on Human Cells

Comparison to correlation ranking. As illustrated in Figure 6, our method identifies novel causal factors for the gene MYC that are not captured by correlation ranking. To quantify the disparity between our model's predictions and correlation ranking, we analyze statistics across 1,868 genes from the Perturb-seq dataset. The average rank correlation between our model's cause scores and correlation-based rankings is

[1]https://www.bnlearn.com/book-crc/code/sachs.interventional.txt.gz

Table 9: **Performance on small graphs.** We measure binary classification accuracy on a pair of nodes to determine whether the method accurately predicts causality. TCD-DL (direct) refers to a variant of our method that trains a model to predict direct causal structures. Each column denotes test datasets with different causal structures and mechanisms. The number of nodes is 10, except for Sachs (Sachs et al., 2005), which has 11. For PC, we use only observational samples.

Method	Linear	MLP	Polynomial	Sigmoid	Sachs
PC	57.2	70.1	69.9	67.6	71.8
GIES	94.3	84.8	70.2	82.3	74.6
TCD-DL (direct)	96.5	86.4	82.3	89.7	75.5
TCD-DL	**96.7**	**88.8**	**83.0**	**90.1**	**76.4**

0.068, indicating low ranking similarity. When comparing the top 20 predictions from each approach, on average only 1.1 genes appear in both sets. Notably, an average of 6.4 genes from our top 20 predictions are validated by the STRING database, underscoring that our model identifies novel causal factors not captured by correlation.

Identifying causes of leukemia-related genes. To further validate our predictions from the K562 Perturb-seq dataset, we use the Human Protein Atlas to identify a set of 29 target genes associated with leukemia (Uhlén et al., 2015). We identify the top 10 causal predictions for each of these target genes, including those with support from the STRING database, and visualize these interactions in Figure 12. We present the resulting GRNs for each leukemia target gene and its predicted causal regulators through network diagrams in Figures 13 and 14. These visualizations highlight the potential regulatory roles of our identified causal genes, providing insights into the predicted interactions driving leukemia. Validation against STRING demonstrates that our approach generates well-supported and highly relevant causal predictions.

Predicted influence of causal genes. We investigate the regulatory influence of each predicted causal gene over leukemia-related target genes in Figure 15. Notably, nucleophosmin (NPM1) is predicted to regulate 25 of the 29 leukemia target genes, receiving support from the STRING database for 21 of these predictions. NPM1 mutations are prevalent in approximately one-third of adult Acute Myeloid Leukemia (AML) cases, leading to an abnormal cytoplasmic localization of the NPM1 protein (Falini et al., 2020). Although NPM1 mutations are primarily associated with AML, recent studies have identified them in a small subset of Chronic Myeloid Leukemia (CML) patients (Young et al., 2021). The prediction that NPM1 regulates a substantial number of leukemia-associated target genes is particularly significant as it provides insights into potential key regulatory mechanisms underlying leukemia pathology. Understanding how NPM1 influences these target genes in CML could reveal critical pathways involved in leukemia progression and help identify novel therapeutic targets.

D Extended Related Works

GRN inference Gene regulatory network (GRN) inference aims to uncover directed causal influences among genes rather than merely identifying co-expression or correlation patterns (Badia-i Mompel et al., 2023). Representative approaches include ARCANE, which employs information-theoretic algorithms (Margolin et al., 2006), and GENIE3, which uses an ensemble of regression trees to predict each gene's expression based on all other genes (Huynh-Thu et al., 2010). While conventional causal discovery methods can be applied to GRN inference, they face significant challenges due to the large network sizes, complex causal mechanisms, and technical noise (Dibaeinia & Sinha, 2020). Recent advancements in sequencing technologies have enabled the collection of interventional data, such as gene knockout experiments, which provide more reliable identification of causal regulators (Replogle et al., 2022). Additionally, recent efforts have focused on developing simulators that generate single-cell gene expression data by modeling the stochastic nature of transcription based on user-provided causal graph structures (Dibaeinia & Sinha, 2020). Our data-driven learning approach leverages these advancements in data collection and simulation, demonstrating the potential of data-driven methods for GRN inference.

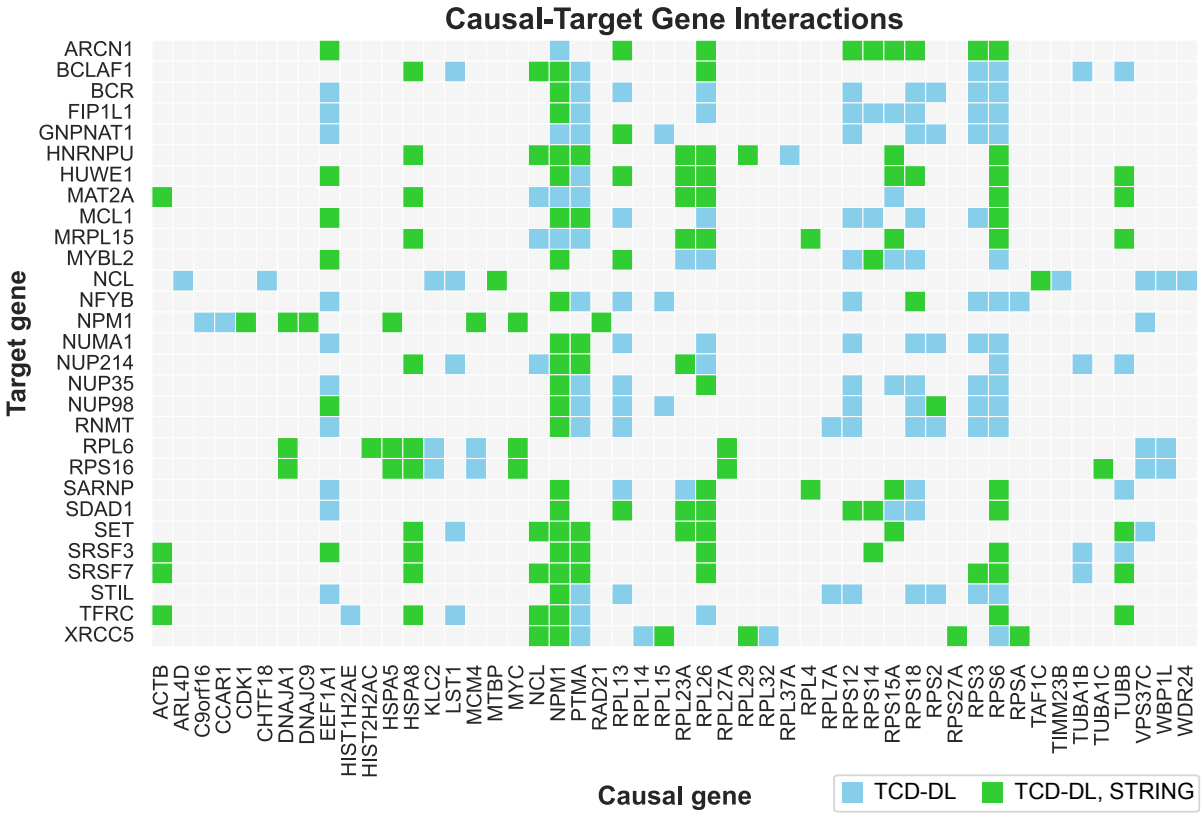

Figure 12: **Predicted causes of leukemia.** The matrix illustrates the predicted causality of leukemia-related target genes by TCD-DL predictions (blue) and TCD-DL predictions supported by STRING (green).

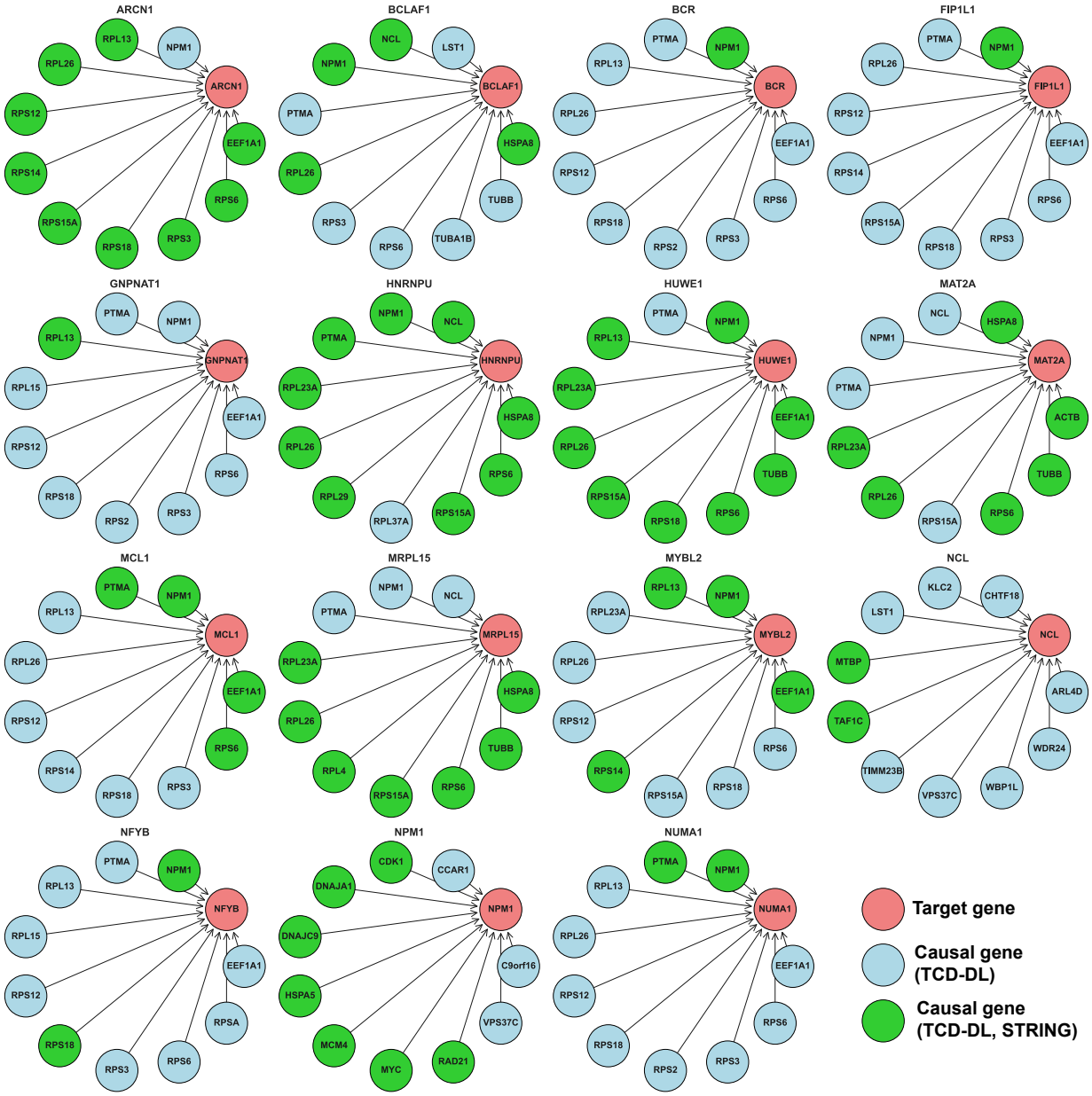

Figure 13: **Predicted causes of a leukemia-related gene.** GRNs illustrate the causal genes predicted by TCD-DL (blue) and TCD-DL predictions supported by STRING (green) for each leukemia-related target gene (pink).

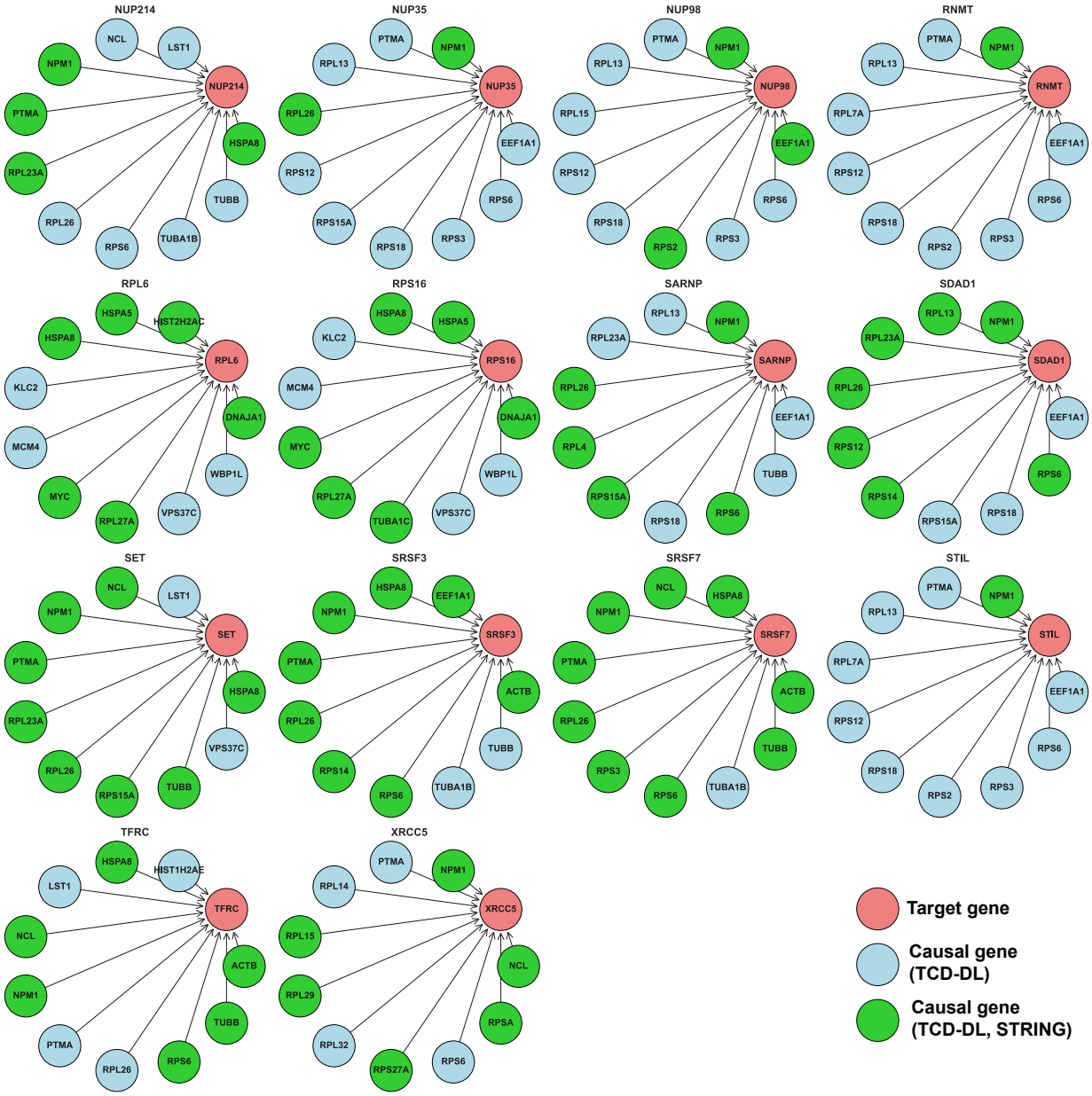

Figure 14: **Predicted causes of a leukemia-related gene.** GRNs illustrate the causal genes predicted by TCD-DL (blue) and TCD-DL predictions supported by STRING (green) for each leukemia-related target gene (pink).

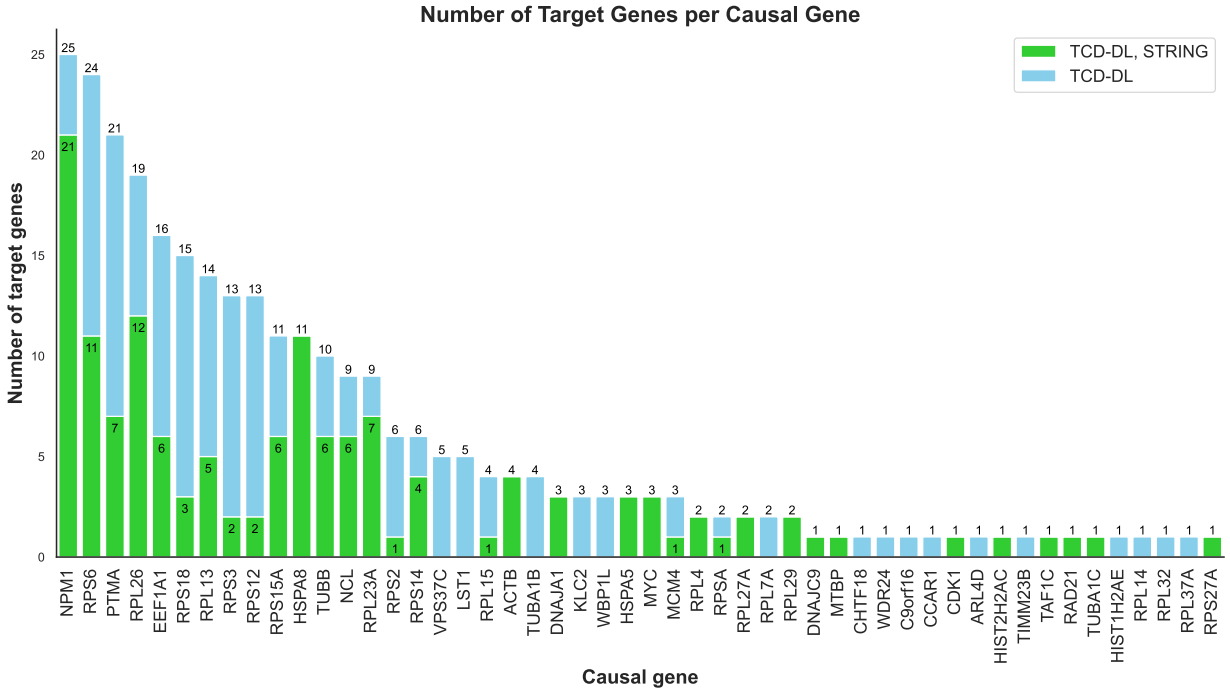

Figure 15: **Predicted influence of causal genes.** The histogram shows the number of leukemia-related target genes predicted to be regulated by each causal gene, with predictions made by TCD-DL (blue) and TCD-DL supported by STRING (green).

Table 10: **Benchmarking results.** Targeted cause discovery performance on E. coli GRN with 1565 genes over varying levels of simulator's observational fidelity. All measurements are expressed as percentages (%).

	Fidelity high			Fidelity medium			Fidelity low		
Method	AUROC	AP	F1	AUROC	AP	F1	AUROC	AP	F1
Random	50.0 ± 0.0	0.5 ± 0.0	0.5 ± 0.0	50.0 ± 0.0	0.5 ± 0.0	0.5 ± 0.0	50.0 ± 0.0	0.5 ± 0.0	0.5 ± 0.0
Correlation	51.1 ± 8.0	0.7 ± 0.2	0.8 ± 0.1	51.0 ± 7.6	0.7 ± 0.2	0.8 ± 0.1	49.8 ± 3.3	0.7 ± 0.1	0.8 ± 0.1
Sortnregress	49.8 ± 0.7	1.4 ± 0.3	1.3 ± 0.4	49.9 ± 0.6	1.4 ± 0.4	1.2 ± 0.4	50.1 ± 0.1	0.7 ± 0.1	0.7 ± 0.2
PMF-GRN	52.6 ± 2.3	0.9 ± 0.1	0.8 ± 0.4	52.9 ± 3.2	1.0 ± 0.2	1.0 ± 0.3	51.5 ± 2.1	1.0 ± 0.1	1.1 ± 0.3
GENIE3	56.0 ± 3.4	2.9 ± 0.8	2.1 ± 0.7	54.3 ± 3.9	2.2 ± 1.1	1.5 ± 0.9	52.2 ± 3.7	1.1 ± 0.2	0.6 ± 0.2
DCD-FG	50.0 ± 0.0	0.6 ± 0.0	1.0 ± 0.0	50.0 ± 0.0	0.6 ± 0.0	1.0 ± 0.0	50.0 ± 0.0	0.5 ± 0.1	1.0 ± 0.0
AVICI	56.5 ± 4.2	1.0 ± 0.2	0.4 ± 0.3	62.7 ± 5.5	3.1 ± 1.7	3.7 ± 2.6	56.5 ± 8.4	1.2 ± 0.9	1.3 ± 1.1
TCD-DL (ours)	**94.6** ± 1.8	**38.6** ± 6.3	**36.3** ± 6.1	**81.7** ± 11.3	**14.0** ± 11.7	**13.4** ± 12.0	**71.5** ± 3.7	**2.4** ± 1.5	**2.0** ± 1.8